

INVESTIGATING THE PHOTODYNAMICS OF  
CONJUGATED POLYELECTROLYTE  
TITANIA FILMS

By

DEREK AUSTIN LAMONTAGNE

A THESIS PRESENTED TO THE GRADUATE SCHOOL  
OF THE UNIVERSITY OF FLORIDA IN PARTIAL FULFILLMENT  
OF THE REQUIREMENTS FOR THE DEGREE OF  
MASTER OF SCIENCE

UNIVERSITY OF FLORIDA

2009

© 2009 Derek Austin LaMontagne

To everyone who ever stopped to smell the pine trees

## ACKNOWLEDGMENTS

Many people have supported me and believed in me throughout my life. I have had so many teachers, coaches, and friends that I cannot name them all, but I would like to specifically mention the people who have helped me here at the University of Florida.

My committee has been helpful in teaching me much about physical chemistry and lasers through the classes I took with them. They have also given me additional guidance when I have come to them with questions. So I would like to thank Dr. Alex Angerhofer for teaching me how to use EPR and for being very approachable with any question I had. I would like to thank Dr. Nicolás Omenetto for teaching me laser fundamentals and helping me calibrate my detector. I would like to thank Dr. So Hirata for teaching me spectroscopy and guiding me to a better fundamental understanding of physical chemistry. And I would like to thank Dr. Valeria Kleiman for being my advisor.

And of course my life would not be fulfilling if it weren't for my friends. So I would like to thank all of my group members: Sevnur, Shiori, Jonathan, Jaired, and Allison. I also should thank some previous group members who helped me a bunch: Daniel and Aysun taught me how to use the laser and setup, and post-docs Gustavo and C.P. were great mentors and even better friends. I also would like to thank all of my fencing teammates for trying to give me a challenge, and my best friend David for being cool.

Chemistry and sports are nice, but family is more important. So I would like to thank my entire family for their support. My dad has always had confidence in me and taught me to be inquisitive in life. My mom has given me everything and always loved me with all her heart. My Nana has always been able to help me with anything, and my brother Dustin is simply the best.

## TABLE OF CONTENTS

	<u>page</u>
ACKNOWLEDGMENTS.....	4
LIST OF TABLES.....	7
LIST OF FIGURES.....	8
LIST OF ABBREVIATIONS .....	10
ABSTRACT.....	11
CHAPTER	
1 BACKGROUND .....	13
Energy Problems and Solutions.....	13
Solar Cell Efficiency .....	15
The Theory of Sensitization .....	16
Conjugated Polyelectrolytes.....	17
Polyelectrolytes as Sensitizers in Solar Cells .....	18
Titanium Dioxide (TiO <sub>2</sub> ).....	20
Excitons.....	23
Energy Transfer .....	23
Excimers.....	24
Aims .....	24
2 FILM FABRICATION .....	26
Film Preparation Methodology: Layer-By-Layer Technique.....	26
Film Thickness Calculations.....	29
3 LASER SET-UP AND SYSTEM MODIFICATIONS .....	32
Steady-State Experiments.....	32
Decay of Films over Time.....	33
Transient Absorption .....	35
Introduction.....	35
Femtosecond Laser Source.....	37
Pump-Probe Set-up .....	39
Detection System.....	41
Modifications .....	42
Atomic Force Microscopy .....	43

4	TRANSIENT ABSORPTION RESULTS AND ANALYSIS .....	47
	Transient Absorption Results for 30 Bilayer Film .....	47
	Bleach.....	47
	Photo-induced Absorption (PIA) .....	50
	Stimulated Emission (SE).....	51
	Assigning Bands .....	53
	Exciton-Exciton Annihilation .....	54
	Exciton Density Calculation .....	55
	Kinetics .....	57
	Data Fitting to Find Rate Constants .....	59
	Exciton Diffusion Length Calculations .....	63
	Effect of Changing Number of Bilayers.....	66
5	CONCLUSIONS AND FUTURE WORK .....	71
	Experimental Discussion .....	71
	Future Experiments .....	72
	Conclusions .....	75
	Exciton Diffusion Calculations .....	75
	PPE-SO <sub>3</sub> Bilayer Film Dynamics.....	76
	Solar Cells .....	76
	LIST OF REFERENCES .....	77
	BIOGRAPHICAL SKETCH.....	83

## LIST OF TABLES

<u>Table</u>		<u>page</u>
2-1	Calculation of film layer thickness .....	31
4-1	Calculation of annihilation rate constant for 30 bilayer film. ....	63
4-2	Calculation of diffusion length for 30 bilayer film.....	65
4-3	Lifetimes of states using single exponential decay fittings. ....	70

## LIST OF FIGURES

<u>Figure</u>	<u>page</u>
1-1 Solar spectrum with PPE-SO <sub>3</sub> <sup>-</sup> overlap zoom shown as the inset.....	14
1-2 Dye-Sensitized Solar Cell (DSC).....	17
1-3 PPE-SO <sub>3</sub> <sup>-</sup> and PDDA <sup>+</sup> polymer repeat units. ....	19
1-4 Diagram of relative band gap energies of polymer/titania/FTO glass. ....	20
1-5 Steady state absorption and fluorescence spectra of TiO <sub>2</sub> films on FTO glass.....	21
1-6 AFM image of TiO <sub>2</sub> on FTO glass, showing mesoporous structure.....	22
2-1 Layer-by-Layer process. ....	27
3-1 Absorption and fluorescence emission spectra of PDDA/PPE-SO <sub>3</sub> films on TiO <sub>2</sub> -coated FTO-glass for 5, 10, 15, 20, 25, and 30 bilayer films. ....	33
3-2 Absorption spectra of FTO-TiO <sub>2</sub> PDDA/PPE-SO <sub>3</sub> films before and after one week.....	34
3-3 Fluorescence spectra of FTO-TiO <sub>2</sub> PDDA/PPE-SO <sub>3</sub> films initially and one week after fabrication. ....	34
3-4 Possible Transient Absorption detectable signals .....	36
3-5 Transient Absorption set-up.....	39
3-6 AFM image for A) 5, B) 10, C) 20, and D) 30 Bilayers.....	44
3-7 AFM “step-height” measurement on 10 bilayer film.....	45
4-1 Complete TA data for 30 BL film excited with 50 nJ pump energy. ....	48
4-2 30 BL film excited with 50 nJ pump energy, plotted selecting time cross-sections to show the dynamics. ....	49
4-3 30 bilayer film excited with 50 nJ pump energy, plotted selecting wavelength cross-sections to show the decays.....	50
4-4 30 BL film excited with 50 nJ pump energy, plotted selecting time cross-sections to show the dynamics. ....	52
4-5 Spectral band assignment from TA data using a Perrin-Jablonski diagram. ....	53

4-6	30 bilayer film bleach signal energy dependence.....	56
4-7	30 bilayers film excited with 50 nJ energy from 420 nm pump beam. ....	60
4-8	30 bilayer film excited with 30 nJ energy from 420 nm pump beam. ....	60
4-9	30 bilayer film excited with 15 nJ energy from 420 nm pump beam. ....	61
4-10	K values over time, for excitation energies of 50 nJ, 30 nJ, and 15 nJ.....	62
4-11	30 bilayer film excited with 12 nJ at 420 nm .....	67
4-12	20 bilayer film excited with 12 nJ at 420 nm. ....	68
4-13	10 bilayer film excited with 12 nJ at 420 nm. ....	69
4-14	5 bilayer film excited with 12 nJ at 420 nm. ....	69

## LIST OF ABBREVIATIONS

BL	Bilayer
CP	Conjugated polymer
CPE	Conjugated polyelectrolyte
EEA	Exciton-exciton annihilation
ET	Energy transfer
FTO	Fluorine-doped tin oxide
FWHM	Full width at half maximum
LbL	Layer-by-Layer
OPA	Optical parametric amplifier
PIA	Photo-induced absorption
PRU	Polymer repeat unit
SE	Stimulated emission
TA	Transient absorption
UV	Ultra-violet
WLG	White light generation/generator
fs	Femtosecond
nm	Nanometer
ps	Picosecond

Abstract of Thesis Presented to the Graduate School  
of the University of Florida in Partial Fulfillment of the  
Requirements for the Degree of Master of Science

INVESTIGATING THE PHOTODYNAMICS OF  
CONJUGATED POLYELECTROLYTE  
TITANIA FILMS

By

Derek Austin LaMontagne

December 2009

Chair: Valeria D. Kleiman  
Major: Chemistry

This work reported in this thesis has used ultrafast transient absorption pump-probe spectroscopy to generate a better understanding of the crucial aspect of energy dynamics within the polymer bilayers and titania-sensitizer interface in multi-bilayer polymer-sensitized solar cells. Photodynamic characterizations are evaluated based on pump excitation dependence and variations in the number of sensitizing bilayers used to increase the light harvesting efficiency and structural stability of these coatings. The sensitizing chromophoric conjugated polyelectrolyte (CPE) chosen for testing was PPE-SO<sub>3</sub><sup>-</sup> because of its ability to form bilayers (with cationic molecules) which can increase total net absorption, because of its recent studies in solution for comparison, and because of its possible potential for photovoltaics and biosensor use. An oppositely charged non-chromophoric polymeric molecule, PDDA<sup>+</sup>, is needed to counterbalance the PPE-SO<sub>3</sub><sup>-</sup> and allow build up of the films' bilayers using electrostatic forces.

Besides increasing the ability of the chromophore to harvest light, the "Layer-by-Layer" synthesis of these films is shown to be an effective and simple approach to streamline production while improving device performance. Increasing the number of

layers is an easy way to increase photon collection efficiency in most cases, and the exact trends and limits to this technique have been evaluated so as to find an optimal layer count before recombination and other quenching processes begin to negatively affect the energy transfer efficiency.

Analysis of ultrafast solid-state transient absorption experimental data on these films has been carried out to describe exciton migration pathways and lifetimes through the polymer layers as well as other photodynamic properties like the electron injection into the titania layer.

## CHAPTER 1 BACKGROUND

### **Energy Problems and Solutions**

The need for inexpensive, clean, and renewable energy is considered one of the greatest problems the world will face during the next century. Harnessing solar energy is regarded as one of the best solutions, because of its global abundance and lack of pollutant byproducts. The goal, then, of engineers and scientists during the next generation will be to optimize solar cells to achieve the most efficient and economically marketable solar cells possible.

In 2008, the United States of America used more than one hundred billion, billion Joules of energy, more than 20% of the global consumption, and less than 7% of that energy came from renewable resources.<sup>1-2</sup> The use of fossil fuels such as petroleum and coal in the U.S.A. alone released roughly six billion metric tons of carbon dioxide into the earth's atmosphere.<sup>1</sup> This behavior is unsustainable on two counts: 1) because there is a limited supply of non-renewable energy sources like fossil fuels, and 2) the burning of such emits harmful gases into the atmosphere which contribute to poorer quality air to breathe as well as enhancing the greenhouse effect that warms the planet. To avoid the catastrophic effects associated with changes in the climate from these anthropogenic problems, scientists must create viable alternatives to compete with the ease of burning fossil fuels.

The amount of energy radiated from our sun from the nuclear fusion reaction of  $H_2$  to He is staggering, some  $4 \times 10^{20}$  Joules every second (W).<sup>3</sup> The intensity of that electromagnetic radiation when it hits Earth is  $1,353 \text{ Wm}^{-2}$ ; however, absorption and scattering from our atmosphere attenuates that to lower than  $1,000 \text{ Wm}^{-2}$  depending on

the angle of incidence. Figure 1-1 shows the solar irradiance spectrum of light which passes through the atmosphere.<sup>3,4</sup> Despite that attenuation, across the globe, and on a yearly basis,  $1.2 \times 10^{17}$  W of potential energy reach the surface,<sup>2</sup> and when one compares this number to the total human yearly demand for energy of  $1.3 \times 10^{13}$  W (roughly 10,000 times less), the true potential for solar cells to solve the energy crisis is seen.<sup>6</sup> Even with the expected increase in world demand due to an increasing population and greater demand from developing countries, covering just 0.2% of the planet's surface with 10% efficient solar cells should provide enough energy for the planet's needs. And this relatively stable energy source is not going anywhere, at least not for more than 10 billion years.<sup>3</sup>

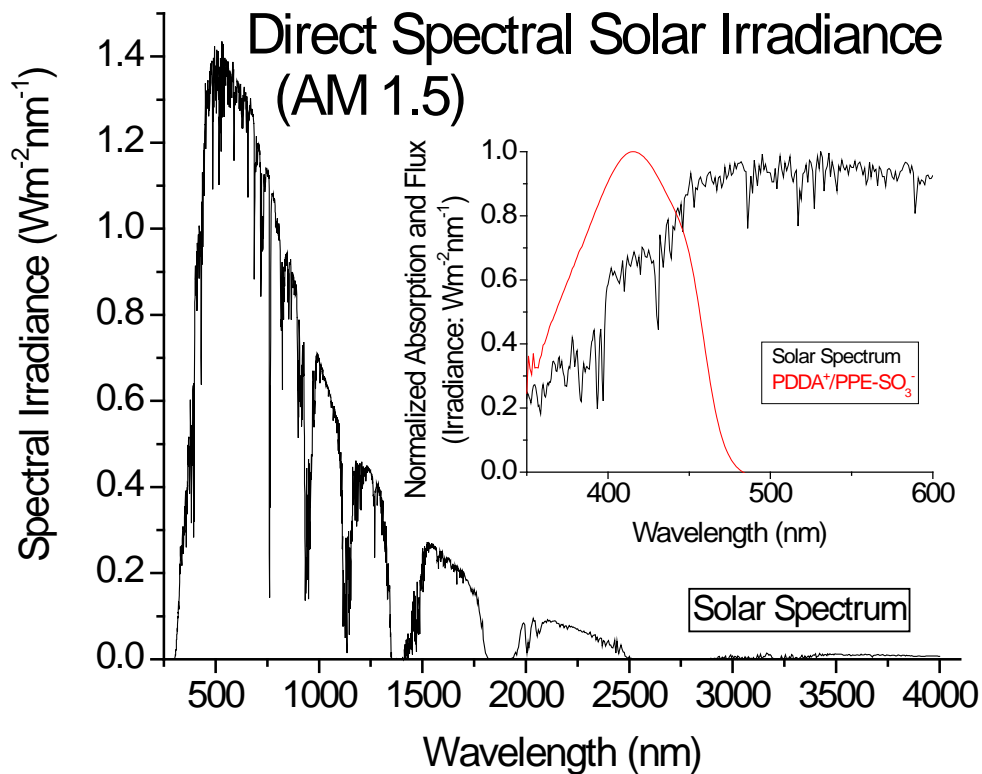


Figure 1-1. Solar spectrum with PPE-SO<sub>3</sub><sup>-</sup> overlap zoom shown as the inset.

## Solar Cell Efficiency

Since one of the main goals of scientists working on solar cells is to improve efficiency, it is best to define what is meant by it. The ideal photovoltaic efficiency ( $\eta$ ) of a device is given by the ratio of the maximum power output to the power input:<sup>3,8,32,53</sup>

$$\eta = \frac{P_{\max}}{P_{in}} = \frac{I_{SC} V_{OC} F_F}{P_{in}} \quad (1-1)$$

where  $I_{SC}$  = short-circuit current,  $V_{OC}$  = open-circuit voltage, and  $F_F$  is the fill factor, which is a measure of the “squareness,” denoting the area, under the I-V curve. To obtain a large  $V_{OC}$ , and thereby a better efficiency, a large energy gap in the chosen absorption material is necessary. Once the choices of absorber and corresponding redox electrolyte are made, the  $I_{SC}$  is given by the photo-induced current of electrons through the system. The photocurrent is influenced by many factors, a few of which will be explored in this proposal in detail, the most notable being the effect of nano-crystalline film morphology, here exemplified by  $TiO_2$  nanoparticles.<sup>8</sup>

As of 2008, the most efficient solar cell on record was a concentrated GaInP/GaInAs/Ge two-terminal cell which can harness air mass 1.5 solar light at an efficiency of  $40.7 \pm 2.4\%$ .<sup>5</sup> Using single cell silicon, the original solar cell semiconductor material, an efficiency of  $27.3 \pm 1\%$  has been achieved over larger areas.<sup>5</sup> Although these cells are very promising, it is important to note that they suffer from one or more of these common problems: they are expensive, they are hard to manufacture on a large scale, they are inflexible, and they cannot coexist with light harvesting plants or animals. Cheap, flexible, polymer-sensitized devices can fix these problems.

## The Theory of Sensitization

Dye-sensitized solar cells (DSCs) are also known as Grätzel cells, after Michael Grätzel who was the first (and still a prominent) developer of them.<sup>6-11</sup> Unlike traditional first generation silicon solar cells, DSCs work by separating the processes of light-harvesting and electron transfer by using a dye layer attached to a semiconductor oxide film.<sup>10</sup> The dye film layer absorbs a photon of light, which then almost immediately ( $<10^{-12}$  s) moves via electron injection into the conduction band of the semiconductor (here  $\text{TiO}_2$ ). An interpenetrating electrolyte couple (often  $\text{I}_3^-/\text{I}^-$ ) then returns the oxidized dye to its ground state by donating an electron in a redox process ( $10^{-10}$  s), two layers of transparent conducting glass on either side establish the electrodes, and an external load completes the circuit. A diagram of this cell is found in Figure 1-2.

If the dye is adsorbed onto a flat surface, it cannot efficiently absorb more than a small percentage of the incoming photons because its cross-sectional volume is essentially two-dimensional, severely limiting the possible absorbance.<sup>8</sup>

$$A = \Gamma \sigma \quad (1-2)$$

This equation for the typical absorbance ( $A$ ) of a dye covered film shows that to increase absorption, one must either increase the sensitizer surface coverage ( $\Gamma$ ,  $\text{mol cm}^{-2}$ ) or find a sensitizer with a better molar cross-section ( $\sigma$ ,  $\text{cm}^2 \text{mol}^{-1}$ ), the latter being simply the molar extinction coefficient multiplied by 1000. To change the former, one can increase the surface roughness by coating the film onto a nanoporous semiconductor, like fractal or nanocrystalline  $\text{TiO}_2$ . Grätzel has shown that a yellow ruthenium dye ( $\text{RuL}_3$ ,  $L = 2,2'$ -bipyridyl-4,4'-dicarboxylate) deposited on "sol-gel" prepared fractal  $\text{TiO}_2$  harvests light with an efficiency near unity at the sensitizer's absorption maximum of 470 nm.<sup>9</sup> Grätzel's group<sup>8</sup> and others<sup>17,34</sup> have recently

demonstrated even greater efficiencies of nanocrystalline TiO<sub>2</sub> from colloidal suspensions as an undoped, wide band gap charge acceptor in DSCs and polymer-sensitized cells.

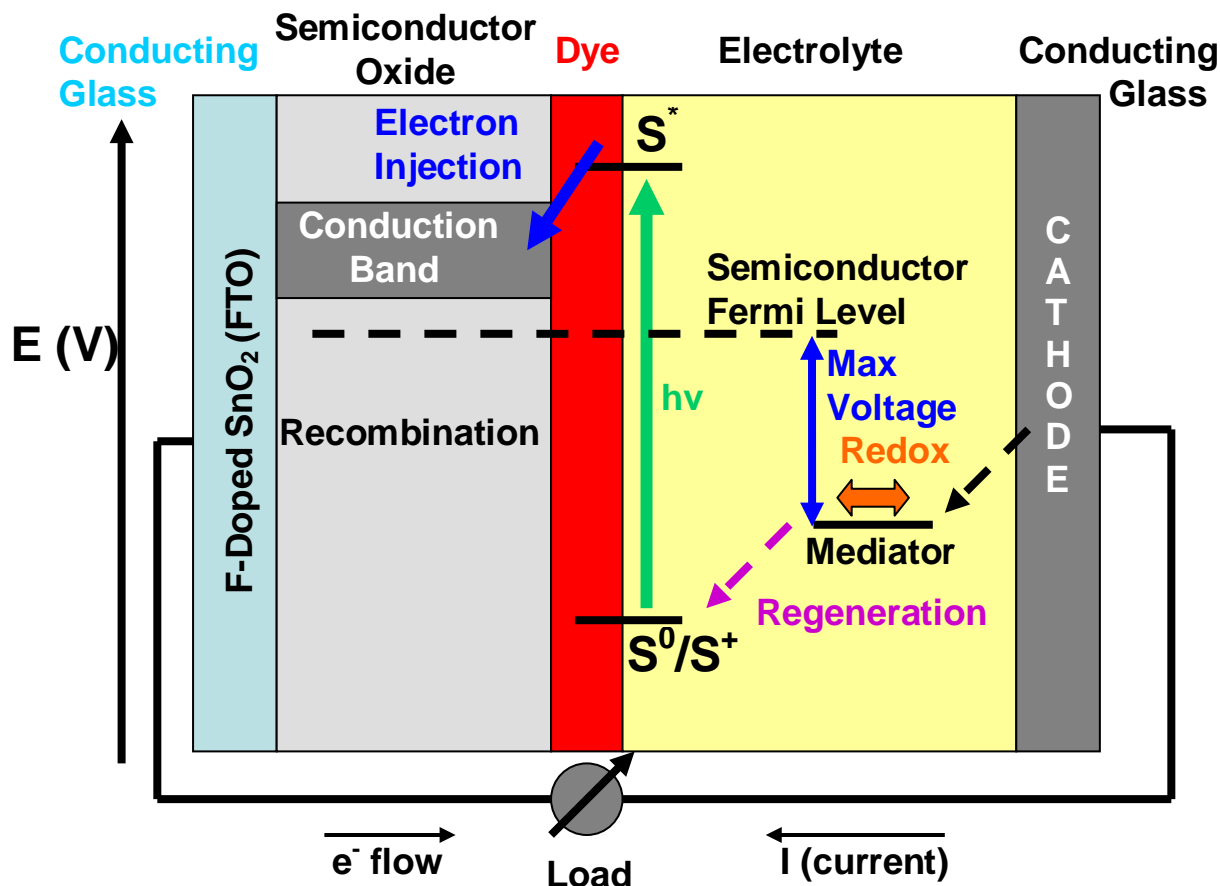


Figure 1-2. Dye-Sensitized Solar Cell (DSC).

Using this idea of sensitization, new molecules are currently being designed to act as the sensitizing layer. One such class of these molecules is conjugated polyelectrolytes, and by building up layers of these to increase absorption, solar cell efficiency may be able to be increased.

### Conjugated Polyelectrolytes

Conjugated polymers (CPs) are a subclass of polymers which demonstrate  $\pi$ -conjugation, which refers to how the  $\pi$ -electron cloud along the covalently bonded

backbone interacts through delocalization, allowing for rapid exciton transfer. As a matter of fact, these polyunsaturated compounds' conductive properties have gained considerable interest since they were first developed by Shirakawa, MacDiarmid, and Heeger in 1977. CPs have been used to replace other semiconductors in such devices as light-emitting diodes, batteries, field-effect transistors, and sensors, specifically in the biological sciences. To elicit a wider range of applications, if one adds ionic side chains to CPs to increase their solubility in polar solvents, then these polymers are called conjugated polyelectrolytes (CPEs).<sup>16,23</sup>

### **Polyelectrolytes as Sensitizers in Solar Cells**

CPEs as the sensitizing (film) layer for use in solar cells and other optoelectronic devices provide manufacturers with the benefits of macroscopic physical flexibility, high tunability via wavelength control from choice of CPE band gap, and in most cases a reduction in cost of materials.<sup>15</sup> Recent studies conducted all over the world,<sup>13,24-26,30-47</sup> include detailed work creating novel conjugated polymers and polyelectrolytes,<sup>14-19</sup> as well as the creation and study of Buckminsterfullerene derivatives and CPE blends for use in optoelectronic devices.<sup>24,41,45</sup>

Extended conjugation in CPEs reduces the minimum energy required to excite an electron from the highest occupied molecular orbital (HOMO) to the lowest unoccupied molecular orbital (LUMO). Moreover, through the addition of specially chosen aryl groups to the backbone of the CPE, the usual range of the band gap for this excitation is in the visible part of the electromagnetic spectrum, making CPEs ideal for solar cells, or inversely tunable for light-emitting diodes.<sup>76</sup>

In particular, the conjugated polyelectrolyte PPE-SO<sub>3</sub><sup>-</sup>, which contains a poly(p-phenylene ethynylene) backbone with anionic 3-sulfonatopropoxy side groups,<sup>21</sup> has

been the focus of numerous studies at the University of Florida.<sup>15,21</sup> PPE-SO<sub>3</sub><sup>-</sup> (Figure 1-3, and often written without the formal charge) demonstrates an ability to be rapidly quenched by cationic species in solution and to form aggregates in certain solutions.<sup>15-17</sup> PPE-SO<sub>3</sub><sup>-</sup> has also been shown to exhibit many useful properties, including strong light absorption and fluorescence, high solubility in biologically favorable solutions, and high mobility of photo-excitations. However, ultrafast studies of the solid-state films made from this polyelectrolyte, which will ultimately be necessary to understand the complete energy transfer picture in this molecule should it be used in applications such as solar cells, have yet to be completed.

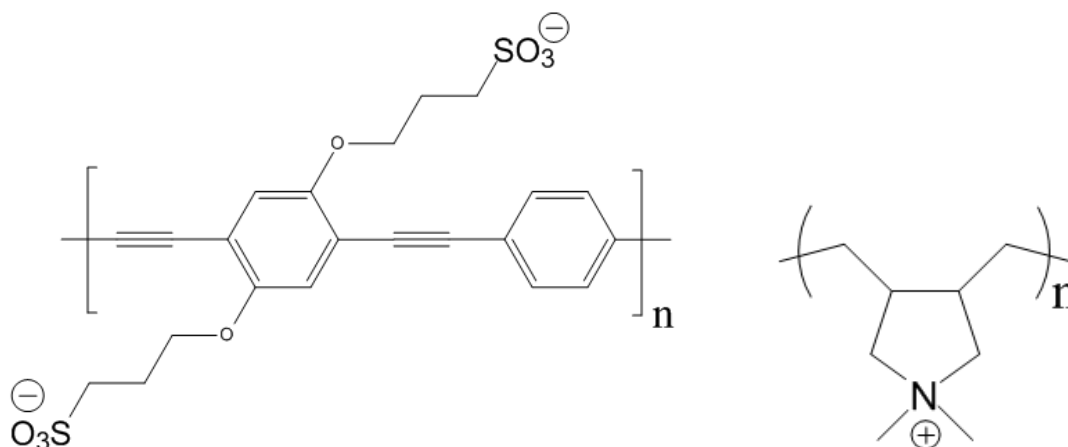


Figure 1-3. PPE-SO<sub>3</sub><sup>-</sup> (left) and PDDA<sup>+</sup> (right) polymer repeat units.

For solar light harvesting, it is necessary to evaluate the spectral overlap of the absorption of PPE-SO<sub>3</sub><sup>-</sup> with the solar spectrum, which can be seen in the inset of Figure 1-1. For optimal, single absorber solar cells, absorption over the entire spectrum creates the most efficient cells. Admittedly, PPE-SO<sub>3</sub><sup>-</sup> only absorbs at a relatively narrow region on the higher energy side of the spectrum. Nevertheless, the potential of this CPE to play a role in optoelectronic devices may still be sought through use in tandem cells or by maximizing the absorption at the wavelengths it does absorb.<sup>6</sup>

To do the latter, a design which maximizes the absorption cross-section has been implemented here by use of a mesoporous TiO<sub>2</sub> interface and multiple bilayer build-up.

### Titanium Dioxide (TiO<sub>2</sub>)

Titanium dioxide, or “titania,” or TiO<sub>2</sub>, comes in multiple forms, but the research reported here started with it as a nanoparticle. Titania is useful in optoelectronic devices such as solar cells for three reasons: 1) it increases the absorption cross-section of sensitizers attached to it compared to having just a flat, two-dimensional sensitizing surface, 2) it facilitates charge transfer through a circuit because of its conductive properties, and 3) it is abundant and a relatively cheap semiconductor.

For an effective solar cell, the HOMO of the CPE must reside within the band gap of the titania, while the LUMO must reside within the conduction band.<sup>69,71</sup> Checking literature (redox) values for PPE-SO<sub>3</sub><sup>-</sup>, TiO<sub>2</sub>, and the substrate, Figure 1-4 is produced.<sup>16</sup>

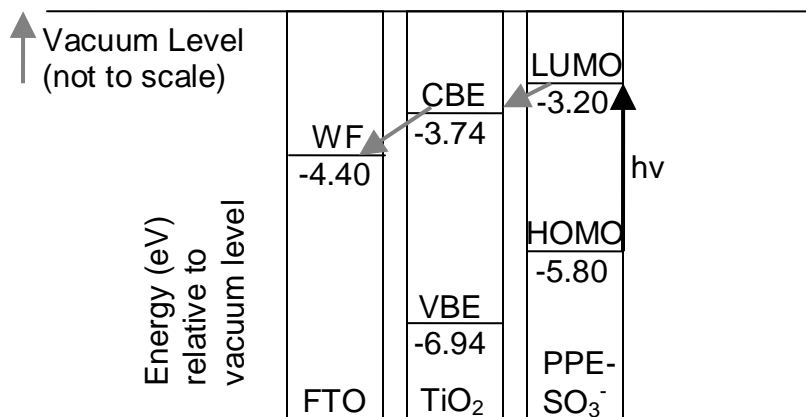


Figure 1-4. Diagram of relative band gap energies of polymer/titania/FTO glass. WF is the work function of FTO glass, CBE and VBE are the conduction and valence band edges of titania, and the difference between the HOMO and LUMO in PPE-SO<sub>3</sub><sup>-</sup> is 2.6 eV = 420 nm, the excitation wavelength. The gray arrows indicate downhill energy migration via electron transfer.

The difference between the valence and conduction band edge energies in titania is 3.20 eV, which corresponds to near-UV absorption, so it will be transparent to 420 nm

excitation. Furthermore, a downhill, favorable electron migration is possible due to the position of the band energies.

The fluorine-doped tin oxide (FTO) glass substrate used in the work reported here was coated with 20 nm diameter nanoparticles (Solaronix®) which were immobilized in their nanocrystalline form through heating. This created a film transparent to the collection wavelengths. FTO-coated glass was chosen for its conductive properties and potential to accept electrons should this system become an optoelectronic device. The titania needs to be heated (sintered) for 45 minutes to generate the anatase nanocrystalline structure on the glass. Figure 1-5 shows the steady state absorption and fluorescence of films produced this way, without any CPE layers.

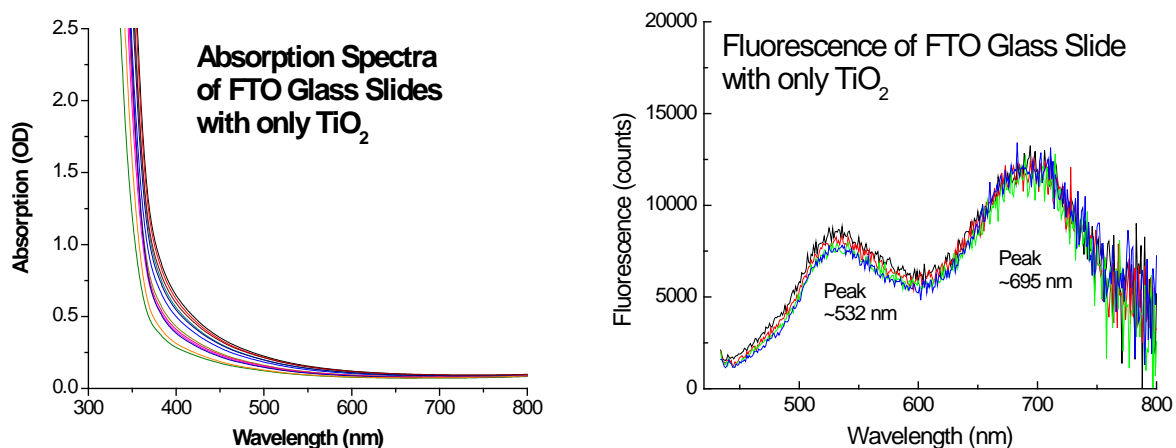


Figure 1-5. Steady state absorption (left) and fluorescence spectra (right) of TiO<sub>2</sub> films on FTO glass. The absorption shows that variations in 14 different titania films show little variation, and all absorb in the UV. The fluorescence with 420 nm excitation for four different spots on the same film show peaks at 532 and 695 nm.

In Figure 1-5, the absorption spectra graph plots 14 different trials, one from each of the slides which were made. They all show UV absorption lower than 400 nm. To assure reproducibility, the front-face fluorescence spectra were collected upon

excitation of four different spots on the same film. It can be seen on the right graph of Figure 1-5 that fluorescence uniformity throughout the film is not a problem. The fluorescence for  $\text{TiO}_2$ , which shows two broad peaks at 532 and 695 nm, has low counts, and detection in the transient absorption spectra is not expected.<sup>67</sup>

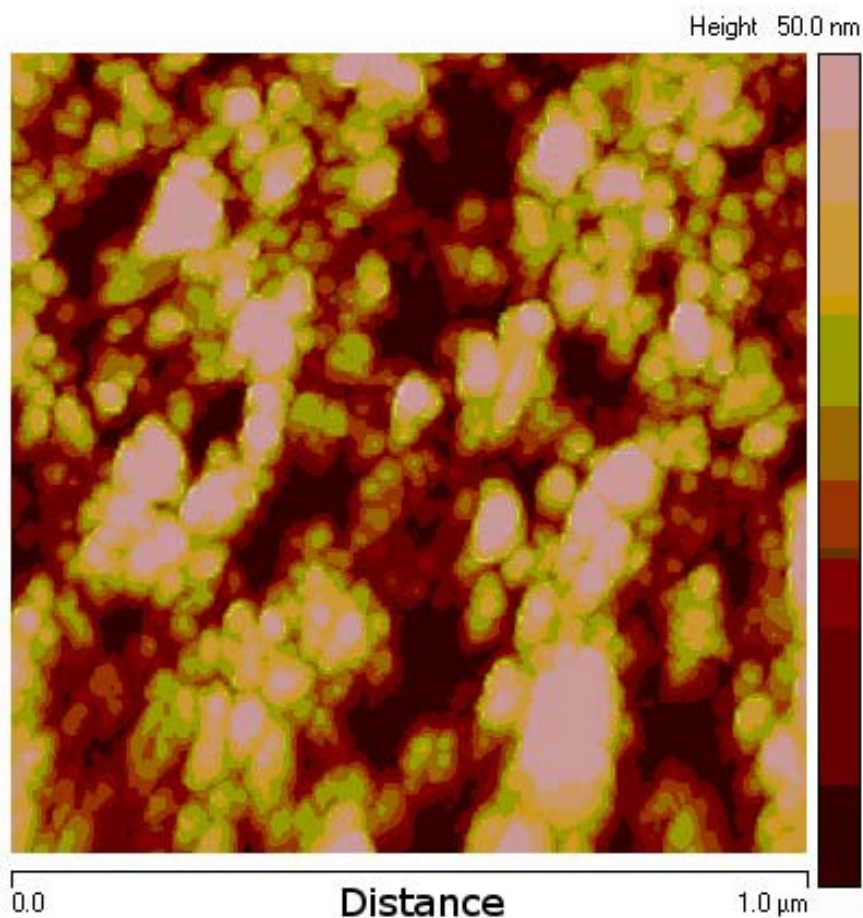


Figure 1-6. AFM image of  $\text{TiO}_2$  on FTO glass, showing mesoporous structure. The raised areas, shown in brighter pink, are the tops of the  $\text{TiO}_2$  nanoparticles, while the darker regions approach the glass substrate, but still contain a layer of  $\text{TiO}_2$ .

Figure 1-6 shows an AFM image of a coating of  $\text{TiO}_2$  nanoparticles on FTO glass, made to the same thickness as that for the studies in this paper. The clusters of titania can clearly be seen, and this porous scaffold is what increases the surface area onto which the CPEs can adhere.

## Excitons

The idea of excitons as excited electron-hole bound pairs comes from molecular crystal studies.<sup>73-74</sup> In those studies, the concept started as a description of the migration of the photo-induced excitation from one molecule to another. In low-energy excited crystal states, the electrically neutral bound pair (exciton) is not a “stationary state,” but instead can be thought of as an excitation “wave” traveling throughout the crystal from the initial point of excitation.<sup>79</sup>

J. I. Frenkel was one of the first people to describe this phenomenon, and the “Frenkel exciton” is used today to describe tightly bound electron hole pairs.<sup>74</sup> In chemistry terms, however, the idea of an exciton can be thought of as a delocalization of the energy in a conjugated polymer. In more detail, however, the exciton can be thought of as new wavefunctions generated from the coupling of chromophores. For PPE-SO<sub>3</sub><sup>-</sup>, the average excitation delocalization length is 5 polymer repeat units.<sup>75</sup>

### Energy Transfer

There are in general two mechanisms by which excitons move through films. The first is by energy transfer in the Coulombic coupling limit, and the second is by energy transfer from electron exchange.<sup>54</sup> Excitons in a triplet excited state usually undergo exchange, which is an intramolecular switching of the donor unit’s excited electron with the acceptor units ground state electron. Because of the relatively slow times for this to occur compared to energy transfer and because triplets are not expected to be seen because of lack of heavy-metal atoms to promote intersystem crossing, this mechanism will not be discussed further in this thesis.

Coulombic energy transfer (ET), however, is a much faster process, and is favored by the shorter lived singlet excited states.<sup>51,54</sup> In this non-radiative ET, Coulombic

interactions between the donor unit and acceptor unit give rise to long range dipole-dipole interaction, and result in transfer of the exciton's energy to the acceptor unit. The rate of ET depends on several factors, including the spectral overlap of the donor's emission and acceptor's absorption and the distance between the units (by an inverse "power of 6" for weak coupling).

### **Excimers**

Because PPE-SO<sub>3</sub><sup>-</sup> exhibits more efficient packing compared to less rigid polymers like polyfluorenes, PPE-SO<sub>3</sub><sup>-</sup> is more likely to form *excimers*. An excimer is a dimer only in the excited state. The fluorescence emission band of an excimer is featureless and red-shifted, and for PPE-SO<sub>3</sub><sup>-</sup> it can be seen in chapter 3 as a broad band at 525 nm. The unaggregated emission band for PPE-SO<sub>3</sub><sup>-</sup> was found to be around 455 nm (it can be seen as a shoulder in the fluorescence of the aggregates). PPE-SO<sub>3</sub><sup>-</sup>'s limited ability to rotate or fold on itself leads to  $\pi$ -stacking, where phenyl rings of neighboring molecules line up face to face, which leads to increased aggregation and formation of excimers.<sup>51,75</sup>

### **Aims**

Characterization of the energy transfer processes in PDDA/PPE-SO<sub>3</sub> films was the overall goal of this research. If one can understand the speed at which these processes take place, one can design better materials for optimal solar cells. Specifically, the experiments being presented here show the excited state lifetimes and photo-dynamic processes of the chosen CPE. In addition, structural, AFM on the film surface and calculation of actual film thicknesses are presented.

It was anticipated that increasing the number of bilayers would increase the absorption in a linear fashion. After a point, however, films that are too thick may

negatively affect the electron injection process because the excitons will be unable to reach the semiconductor ( $\text{TiO}_2$ ) and therefore will not be able to cleave and contribute to the circuit of the cell. Finding this limit is important for designing better solar cells.

After studying  $\text{PPE-SO}_3^-$  in depth, certain trends and equations were evaluated, which help give a better picture of the energy transfer process in polyelectrolyte films in general.

## CHAPTER 2 FILM FABRICATION

Steady state absorption, emission, and time-resolved femtosecond transient absorption (TA) were the focus of the lab work in characterizing these films. However, the production of the test films in a relatively easy and efficient way was also demonstrated.

### **Film Preparation Methodology: Layer-By-Layer Technique**

In order for these films to be produced on a large scale, as is the goal should they be used in the photovoltaics industry, the production method must be as free from unnecessary stress as possible. For this reason, spin-coating and evaporation techniques, which require significant mechanical energy use, were relinquished for the less strenuous method of “Layer-by-Layer” deposition (Figure 2-1).<sup>49</sup> The “Layer-by-Layer” (LbL) technique can be done with no additional equipment other than the polymers, vials, solvent, pipettes, tweezers, and a dedicated scientist. No heating or temperature fluctuations are necessary. Neither are any mechanical devices, although this process can surely be automated for reproducibility. It should be noted however that a robotic dipper is available, but due to its rapid use of solvents and openness to the atmosphere, thereby causing increased aggregation and titania degradation due to dissolved water, this resource was not employed.

To start the Layer-by-Layer process, a preliminary coating of  $\text{TiO}_2$  is doctor-bladed and sintered at  $450^\circ\text{C}$  for 30 minutes (to change  $\text{TiO}_2$  from the rutile to the more easily adsorbing anatase surface)<sup>27</sup> onto a 1.75 cm x 1.26 cm area on a clean FTO-coated soda lime glass slide.<sup>51</sup> The FTO-glass is cleaned via sonication in solutions of soap, deionized water, acetone, and isopropanol, followed by 20 minutes in a plasma

cleaner. After taking a steady state absorption spectrum on a film run in parallel (for later background correction), the slides were then ready to be coated with the first polyelectrolyte layers.

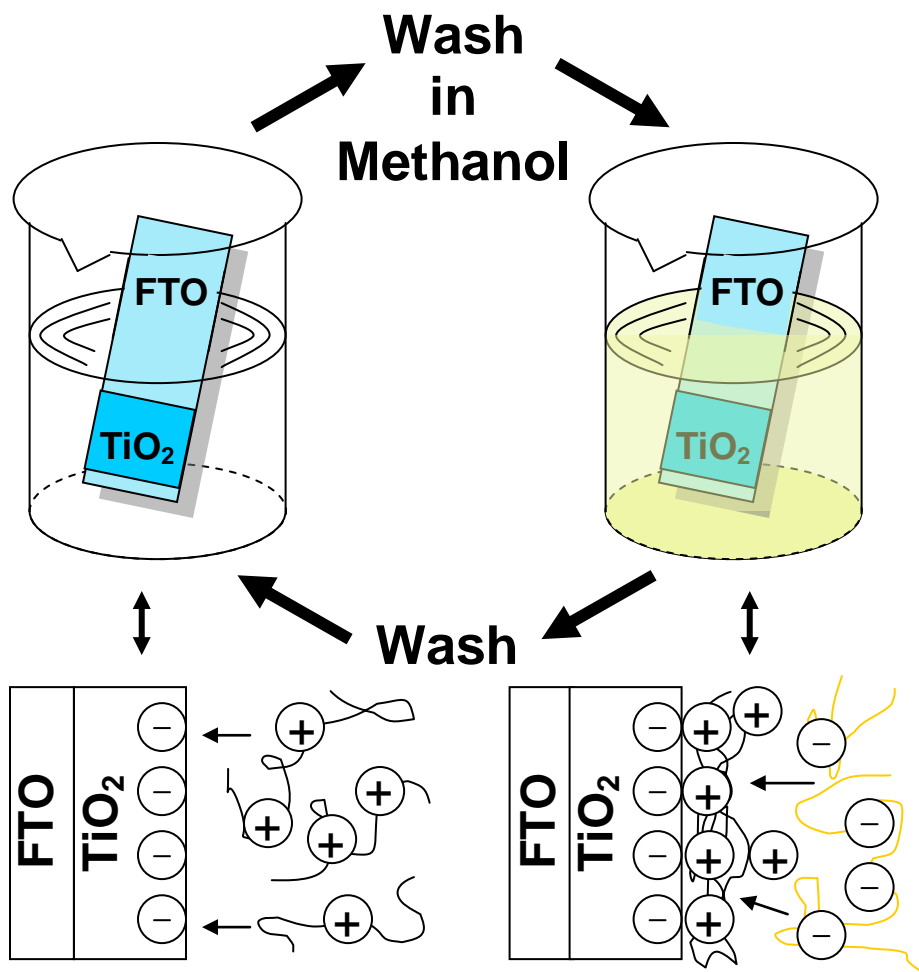


Figure 2-1. Layer-by-Layer process.

The adsorption experiments involve using alternating layers of oppositely charged polymers to create bilayers which can theoretically be built to any thickness. As mentioned before, the polyelectrolyte chromophore chosen was PPE-SO<sub>3</sub><sup>-</sup> because of its degree of study in solution for comparison,<sup>21</sup> as well as its promise to be used for fabrication of sensors for ions, peptides, nucleic acids, and proteins.<sup>15</sup> To create a nanostructured multilayer which binds electrostaticly, a non-chromophoric aliphatic

polycation, poly(diallyldimethylammonium chloride), or PDDA<sup>+</sup>,<sup>52</sup> was chosen so as not to interfere with the PPE-SO<sub>3</sub><sup>-</sup> (Figure 1-3).

The cationic layer of PDDA<sup>+</sup> was added first to the slide to adsorb onto the anatase form of TiO<sub>2</sub>. To achieve this, one allows the bottom half of the slide containing the TiO<sub>2</sub> surface to soak in a 1mM solution (in methanol) of the counter cation PDDA<sup>+</sup>. After the prescribed wait period of 25 minutes, the slide is then run through three separate methanol washes (3, 1, and 1 minutes), and finally placed into a 1mM solution (in methanol) of the PPE-SO<sub>3</sub><sup>-</sup> anion polyelectrolyte for 25 minutes. After this layer is added, the slide is run back through clean methanol vials and a new bilayer is ready to begin. The total time for one bilayer to be coated is one hour.

Variations in the soak times were considered but because this study focused on the photodynamics, previous working methods were decided to be better than new, untested soak times. It is expected, though, that increasing the thickness of a single bilayer merely creates a greater number of aggregated states as the polymers cluster together on the film. Aggregation may then quench the excitons of PPE-SO<sub>3</sub><sup>-</sup> in a nonlinear fashion with increasing layer thickness, which is undesirable.

The relatively short time of 25 minutes was chosen in order to limit aggregation while still providing complete film layer coverage. Using this strategy, an individual bilayer thickness should be about 2 to 3 nm, and films containing 100 or more bilayers can be fabricated. But for these experiments, the focus was to create films of 5, 10, 15, 20, 25, and 30 bilayer thicknesses (in order to compare exciton diffusion before it reaches its limit, expected to be under 30 bilayers)<sup>13</sup> and evaluate their linear optical properties.

## Film Thickness Calculations

Although the thickness of the titania layer of a few microns determines the main scaffold on which the films are built, it is possible and useful to calculate the relatively small additions to that thickness generated by the polymer bilayers. The Layer-by-Layer process implemented here was expected to generate thickness as low as a few nanometers upwards of 50 nm.<sup>57,58</sup> Thicknesses are affected by length of time in the dipping solution, concentration of the solution, and the amount of interlayer diffusion which takes place during the coating process. It was further expected that if the interlayer diffusion is low, then a linear relation would be seen as bilayers were built up.<sup>59,60</sup>

The absorbance of a 10  $\mu\text{M}$  PPE-SO<sub>3</sub><sup>-</sup> in methanol solution at its maximum absorption wavelength of 420 nm is 0.57, although this value has been found to vary between 0.40 and 0.60 for different stock solutions.<sup>75</sup> Using  $A = 0.57$  and the fact that it was taken in a 1 cm cuvette, one can calculate the molar absorption coefficient ( $\epsilon$ ) from:

$$A = \epsilon lc \quad (2-1)$$

Where “A” is the absorbance, “l” is the length of the cuvette, and “c” is the concentration. Equation 2-1 is a form of the Beer-Lambert Law.<sup>54</sup> From this equation, the molar absorption coefficient was calculated to be about 57,000  $\text{M}^{-1}\text{cm}^{-1}$ . It should be noted that this value is based on one polymer repeat unit (PRU) because that was used in the solution studies, although absorption occurs in a chromophore longer than one PRU.<sup>75</sup> It is standard convention to use one PRU values in most calculations, despite the fact that a chromophore covers about 5 PRU for PPE-SO<sub>3</sub><sup>-</sup>.<sup>51</sup> And although this  $\epsilon$  value is for the unaggregated CPE in methanol solution, it was used in the calculation of thickness for the solid state films which show aggregation because the films were

produced using methanol solution, because studies to determine  $\epsilon$  in a solution with aggregation have not yet been done, and because changes in absorption due to aggregation have been shown to be hard to calculate due to lack of data reproducibility.<sup>29</sup>

The background corrected (TiO<sub>2</sub> and glass subtracted) absorption maxima of the films at the chosen bilayer numbers are shown with the calculated thickness in Table 2-1. The absorption spectra can be found in the next chapter in Figure 3-1.

An example of the calculation, using the 30 bilayer film, is as follows:

$$l = \frac{A}{\epsilon c} = \frac{0.492}{(57000 M^{-1} cm^{-1})(2.11 M)} \approx 4.10 \times 10^{-6} cm = 4.10 \times 10^{-8} m = 41.0 nm \quad (2-2)$$

The molecular weight was taken as the formula weight for a repeat unit of PPE-SO<sub>3</sub><sup>-</sup>, 474.51 g for C<sub>22</sub>H<sub>18</sub>O<sub>8</sub>S<sub>2</sub> (sodium was the original counter-ion, but during LbL it reenters solution when PDDA<sup>+</sup> is adsorbed), and the generally accepted value of film densities was also used, which is 1 g/cm<sup>3</sup>.<sup>72</sup> This density value used is an assumption, but Malone and Albert have shown that a wide range of polymers all yield this value within 25% error.<sup>72</sup> Because the polymers used here are CPEs with charges, this assumption may contain an even larger error, but any more exact value has yet to be found, so 1 g/cm<sup>3</sup> was used in the calculations. Thus, the polymer repeat unit concentration value was determined to be:

$$\frac{1 g}{1 cm^3} \left[ \frac{10^3 cm^3}{1 dm^3} \right] \left[ \frac{1 mol}{(474.51 g)} \right] \approx 2.11 M \quad (2-3)$$

The absorption values found in Table 2-1 really only describe how much PPE-SO<sub>3</sub><sup>-</sup> the incident beam (during steady-state absorption studies) encounters, and makes no distinction about whether or not there are large distances between the CPEs. It is

possible that the beam passes through multiple TiO<sub>2</sub> particles which are each coated with a few nanometers of thickness so that the sum of the thicknesses equals the final thickness; however, it is unlikely because it assumes that there are empty spaces underneath nanoparticles in the TiO<sub>2</sub> scaffold. Once the TiO<sub>2</sub> was heated, it became the more interconnected anatase form, which inhibits penetration into the TiO<sub>2</sub>, but creates a large, rough surface area to promote adsorption. It is therefore assumed that the entire thickness of the film is connected (not found as separate, disconnected vertical layers) on the outermost side of the scaffold.

It is further assumed that the flexible PDDA<sup>+</sup>, because it is a less bulky polymer than PPE-SO<sub>3</sub><sup>-</sup>, will not separate the PPE-SO<sub>3</sub><sup>-</sup> layers by more than one or two nanometer thickness; thus in Table 2-1, the thicknesses shown may only be that of a single layer (of PPE-SO<sub>3</sub><sup>-</sup>), not an entire bilayer. The true bilayer thickness is unknown because PDDA<sup>+</sup> did not absorb, but it can be estimated to be double that of a single layer.

In Table 2-1, the increase in thickness is relatively linear, with an increase of about 7 nm per 5 layers, or about 1.3 nm per layer. This indicates low interlayer diffusion during the coating process.

Table 2-1. Calculation of film layer thickness

Number of Bilayers	Max Absorption (OD)	Thickness (nm)	Thickness per layer (nm)
30	0.492	41.0	1.37
25	0.376	31.3	1.25
20	0.308	25.6	1.28
15	0.236	19.6	1.31
10	0.165	13.7	1.37
5	0.081	6.7	1.34

## CHAPTER 3 LASER SET-UP AND SYSTEM MODIFICATIONS

The experiments in this work only looked at the FTO/titania/CPE interface, which could potentially act as the photoanode in a solar cell, as in Figure 1-2. The dynamics of the photoinduced sensitizer excitation of an electron from the HOMO to LUMO of the conjugated polyelectrolyte and subsequent electron injection into the Fermi level of the TiO<sub>2</sub> acceptor were evaluated. Although not part of the investigation in this proposal, a fully functional solar cell would need to have an electrolyte redox couple such as an I<sub>3</sub><sup>-</sup>/3I<sup>-</sup> or a hole transporting layer to effectively produce a circuit.<sup>11</sup> It is possible that future tests on the complete cells using solar simulators can be done, possibly through a collaboration.

### **Steady-State Experiments**

Steady state absorption spectra were taken on a UV-Vis Varian-Cary 100 spectrometer. The wavelength range was detected from 300 nm to 800 nm by 1 nm intervals to cover the visible light spectrum. Fluorescence emission spectra were taken using a Jobin-Yvon Spex-Fluorolog-3 in the range from 430 nm to 800 nm.<sup>50</sup> All experiments were done at room temperature, and an average of four spots on the films was used as the final spectral value.<sup>51</sup>

Figure 3-1 shows steady state data for PDDA<sup>+</sup>/PPE-SO<sub>3</sub><sup>-</sup> films with the glass/TiO<sub>2</sub> background subtracted out. The absorption peak at 420 nm will be the wavelength of pump beam excitation in the TA setup. The emission spectra were excited with 420 nm. It should be noted that the 525 nm fluorescence peak is due to emission of the aggregate form, which is more prevalent at a higher number of bilayers.<sup>51</sup> The unaggregated peak, at 455 nm, is seen as a shoulder. Absorption rises

linearly, while fluorescence rises monotonically but not linearly with increasing bilayers. This can be seen in the inset graph of Figure 3-1, which includes two points per number of bilayers (absorption: 420 nm; fluorescence: 515 nm) because there were two films created for each number of bilayers.

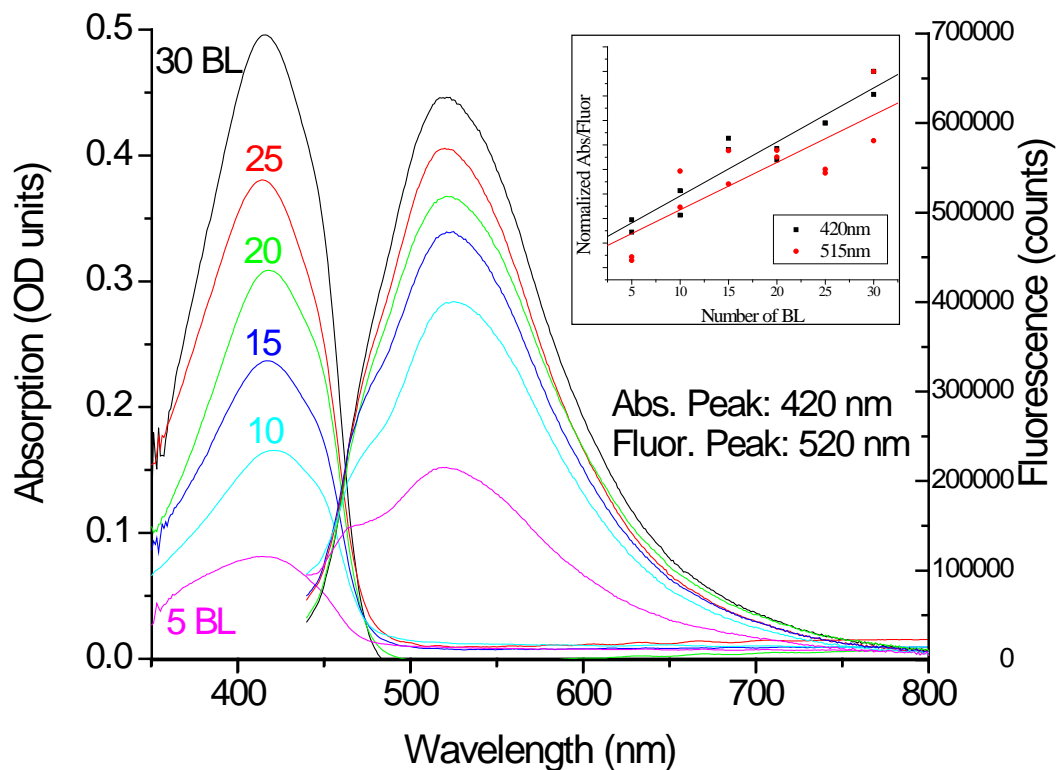


Figure 3-1. Absorption and fluorescence emission spectra of PDDA/PPE-SO<sub>3</sub> films on TiO<sub>2</sub>-coated FTO-glass for 5, 10, 15, 20, 25, and 30 bilayer films. Each line is an average of four scans at different points in the film. Excitation for the fluorescence was 420 nm. TiO<sub>2</sub>/FTO backgrounds were subtracted for the absorption. Inset shows absorption/fluorescence rises, including points from an additional set of films.

### Decay of Films over Time

A transient absorption study of these films would not be possible if they naturally degraded over time. Therefore, the steady state absorption and fluorescence spectra

were monitored every week. The first week's results are found in Figures 3-2 and 3-3.

It should be noted that during the synthesis process, two films were made for each

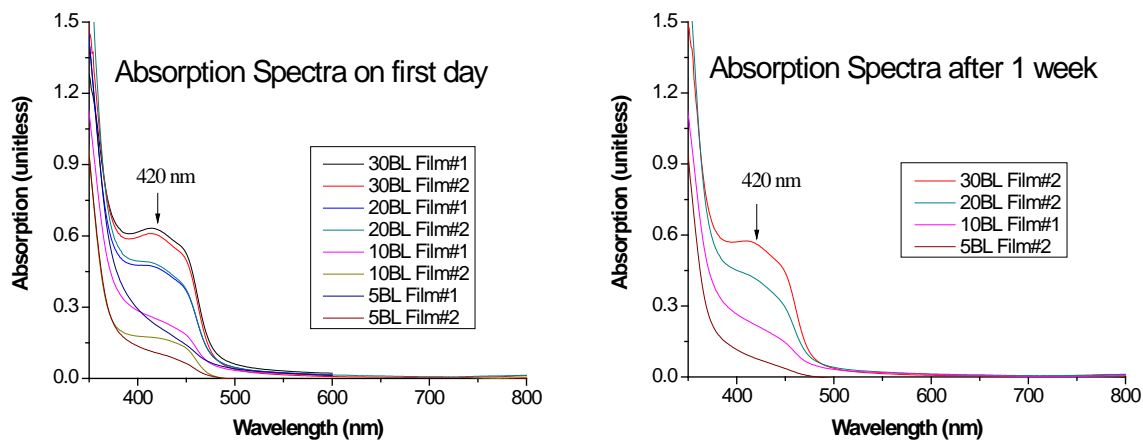


Figure 3-2. Absorption spectra of FTO-TiO<sub>2</sub> PDDA/PPE-SO<sub>3</sub> films before (left) and after (right) one week. No background subtraction was done here only to show effect of glass/titania. Each curve is the average of four scans. The right graph just shows the best films out of the two that were made at each bilayer number. Curves shown are for 5, 10, 20, and 30 bilayers.

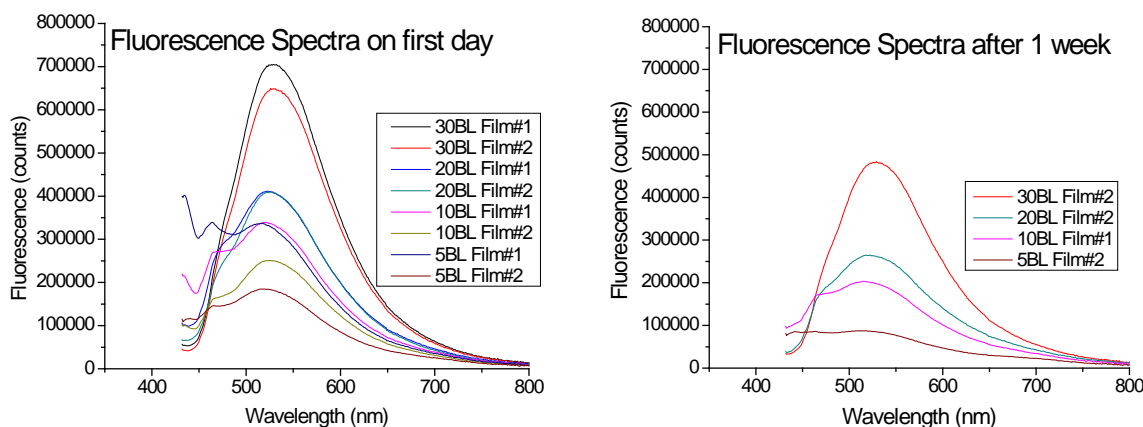


Figure 3-3. Fluorescence spectra of FTO-TiO<sub>2</sub> PDDA/PPE-SO<sub>3</sub> films initially (left) and one week after (right) fabrication. No background subtraction was needed because TiO<sub>2</sub> fluoresces relatively weakly.  $\lambda_{\text{excitation}} = 420 \text{ nm}$ . The right graph shows just the best films, while the left graph shows some unaggregated signal around 455 nm. Each curve is the average of front-face collected data at four different locations on the film. Curves shown are for 5, 10, 20, and 30 bilayers.

bilayer number. It was then decided based on the spectral shape and amplitude which of the two was better, and that one was used in experimentations; hence, why the graphs on the right for “after one week” only show one film per bilayer number – the graphs only contain data for the “better” films. Again, the fluorescence (excited with 420 nm) is dominated by the 525 nm signal from the aggregated PPE-SO<sub>3</sub><sup>-</sup>.

The unaltered absorption spectra (Figure 3-2, without the FTO-TiO<sub>2</sub> background subtraction), is shown for reference purposes to demonstrate how much the glass and titania themselves absorb. One week after fabrication, the spectra barely change. In Figure 3-3, each film’s fluorescence spectra decayed by roughly one third of the original just after the first week. It is believed that this is due to degradation of the titania support structure from water in the atmosphere.<sup>65-66</sup> This effect was limited as much as possible by storing the films in a vacuum desiccator at all times when not in use. The TA experiments were also run as soon as possible after film fabrication.

## **Transient Absorption**

### **Introduction**

Transient absorption spectroscopy experiments, also known as “pump-probe” spectroscopy, rely on two ultrashort pulses, a “pump” and a “probe.” The pump is more intense, and perturbs the sample at some time, called “time zero,” while a whitelight probe beam monitors the excited state dynamics through changes in its absorption spectrum. The relative time between the two pulses is varied using an optical delay stage to see the time-resolved characteristics in the spectrum.<sup>50</sup>

After the initial excitation, parts of the whitelight probe spectrum will either show an increase or decrease in absorption. As shown in Figure 3-4, increase in absorption is due to photo-induced absorption into a higher excited state, while a decrease in

absorption may be due to either ground state bleaching (fewer molecules in  $S_0$  to absorb) or because of stimulated emission at the wavelengths of fluorescence. Unlike fluorescence which is a spontaneous process, stimulated emission depends on the fluence of the excitation beam.

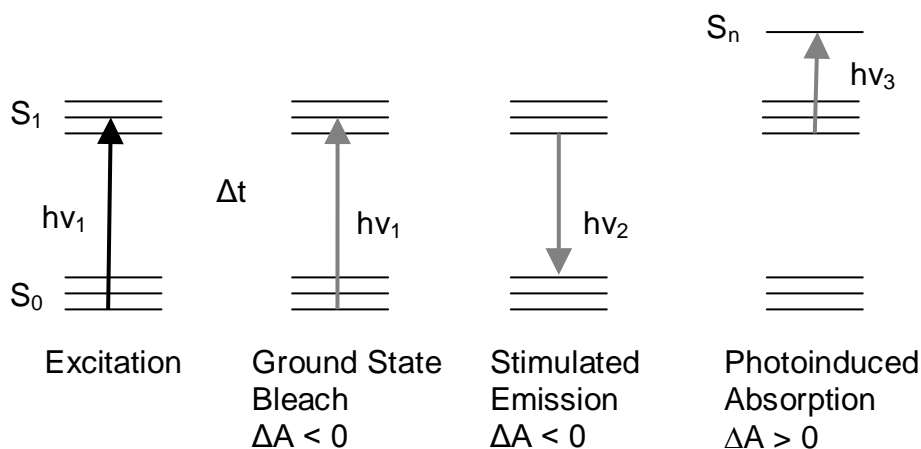


Figure 3-4. Possible Transient Absorption detectable signals.

The transient absorption technique has been used before on all sorts of materials, including work on  $C_{60}/GaAs$  bilayers<sup>24,40,41</sup> and nanosecond studies on polyelectrolytes,<sup>51</sup> but an ultrafast TA experiment that explores the dynamics of the chosen polyelectrolyte film on a titania scaffold has not yet been done. Determining how far and how fast the photo-induced excitons can travel will also demonstrate the quality of the films, because it is expected that if aggregation is more prevalent, then the exciton lifetime, and thereby anode efficiency, will be reduced somewhat.

To create a higher irradiance to increase the number of excitons created, the pump beam was focused at the sample position using an off-axis parabolic mirror (focal length = 15.24 cm) onto the surface of the films to be tested. The exciton dynamics can be studied through analysis of time-resolved data from exciton-exciton annihilation, while monitoring the spectral change in absorption as a function of time.

For the TA experiment, wavelength intensity data are collected after a grating monochromator by a CCD detector in the form of “relative change in transmission,” or  $\Delta T/T$ . Transmission and absorption are related through Equation(s) 3-1.<sup>50</sup> The intensity of the probe beam ( $I$ ) is detected with and without the pump beam on (turned on/off with a chopper). The reference beam ( $I_0$ ), an identical beam to the probe which does not go through the volume excited by the pump, is used to limit shot-to-shot power fluctuation noise. The signal is given by Equation 3-2.<sup>50</sup>

$$A(\lambda) = \log \frac{I_0(\lambda)}{I(\lambda)} = -\log T(\lambda) \quad (3-1)$$

$$T(\lambda) = \frac{I(\lambda)}{I_0(\lambda)}$$

$$\frac{\Delta T}{T} = \frac{T_{pump} - T_{nopump}}{T_{nopump}} = \frac{\frac{I_{t,pump}}{I_0} - \frac{I_{t,nopump}}{I_0}}{\frac{I_{t,nopump}}{I_0}} = \frac{I_{t,pump}}{I_{t,nopump}} - 1 \quad (3-2)$$

$$\Delta A = -\log \left( \frac{\Delta T}{T} + 1 \right) \quad (3-3)$$

Finally, the change in absorption (in mOD) is calculated by Equation 3-3.

### Femtosecond Laser Source

Ultrafast (~55 fs) laser light pulses for use in the transient absorption experiments were created using a commercially available laser system made by Spectra Physics®. A “Millennia,” a continuous-wave neodymium:yttrium vanadate (Nd:YVO<sub>4</sub>) solid state laser, provides 532 nm output with powers of several Watts. The Millennia pumps a mode-locked titanium-doped sapphire oscillator called a “Tsunami” which produces pulses centered at 790 nm that are 35 nm wide (FWHM) and ~35 fs in time, have a 82

MHz repetition rate, and which are used to seed a regenerative amplifier called a “Spitfire.”<sup>77</sup> The Spitfire is a titanium-doped sapphire regeneration amplifier pumped by an “Evolution X,” a Q-switched neodymium:yttrium lithium fluoride (Nd:YLF) diode-pumped laser.<sup>50</sup> The Evolution X provides 6 W of power at 527 nm and a repetition rate of 1 kHz. Inside the Spitfire, the pulses undergo stretching, amplification, and then compression, before they are released with an energy of 0.840 mJ per pulse centered at 795 nm with a pulse width of 55 fs and repetition rate of 1 kHz. This energy is split in half using a beam splitter for use in two independent OPA systems.

The 0.420 mJ energy after the first beam splitter passes another beam splitter which takes 4% to be used for TA whitelight generation. The 96% of the 0.420 mJ has a Gaussian beam spectral output centered at 795 nm, and must be changed to a wavelength at which the sample absorbs, so an optical parametric amplifier (OPA) was used for wavelength control. This OPA provides near transform-limited and high energy output pulses.<sup>50</sup> Unlike a laser, an OPA’s gain comes from nonlinear processes such as second harmonic generation (SHG), fourth harmonic generation (FHG), sum frequency mixing (SFM), and difference frequency mixing (DFM).<sup>77</sup> In these processes, a whitelight continuum seeds a  $\beta$ -barium borate (BBO) crystal as the nonlinear medium. Using these processes and a proper selection of the signal or idler beam, phase matching, polarization, and number of harmonic crystals, any desired wavelength within a range of just under 300 nm to just above 10  $\mu\text{m}$  can be generated.<sup>50</sup> The excitation wavelength chosen here (420 nm) is based on the most optimal absorption of the molecules as seen in their absorption spectra (Figure 3-1), and is created by using two BBO crystals to generate the FHG of the idler beam. An adjustable waveplate was

fixed inside the OPA before the SHG crystal to allow for control of the output energy for later use in energy-dependent studies.

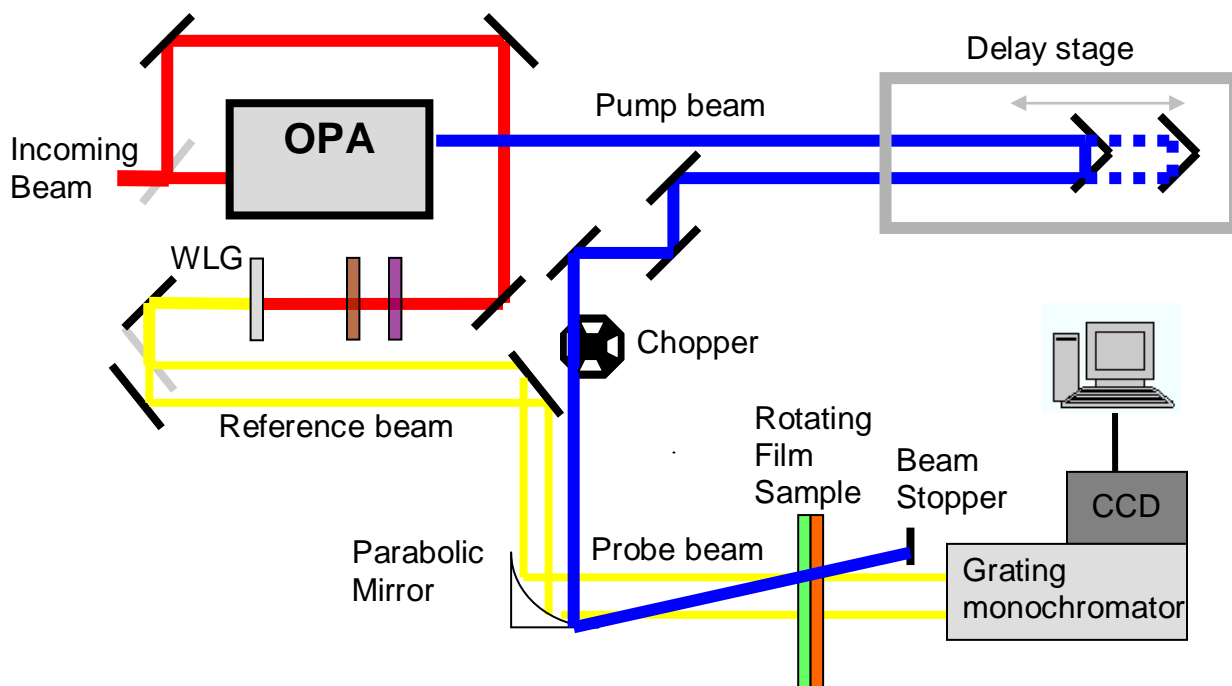


Figure 3-5. Transient Absorption set-up. The sample and WLG ( $\text{CaF}_2$  window) are on rotating stages. An 800 nm wavelength, 1 kHz repetition rate, 0.42 mJ beam splits to generate WL and seed the OPA. Prior to reaching the WLG, the beam is attenuated using a waveplate and polarizer. A 420 nm pump beam is made through second and fourth harmonic generation of the OPA idler beam. Pump, probe, and reference are focused on the near side of the film using an off-axis parabolic mirror, then photons are collected using a spectrograph and CCD (charge-coupled device) camera.

### Pump-Probe Set-up

The 4% of the 0.420 mJ energy (that was separated before the OPA) passes through a waveplate (to lower the energy to about 4  $\mu\text{J}$ ) and polarizer (set to the magic angle,  $54.7^\circ$ ) and is then focused (using a 100 mm focal length lens) onto the far side of a 1 inch diameter, 1.5 mm thick rotating  $\text{CaF}_2$  window to generate a supercontinuum (white light spectrum). Rotating the window removes shot-to-shot fluctuations, while focusing on the far side of the window avoids unwanted dispersion effects. After

collimation by an off-axis parabolic mirror, this whitelight beam is then split 45:55 into a probe and reference beam. The reference passes through two extra mirrors, so because of losses from less than 100% reflectivity in the mirrors, it needs about 55% of the whitelight from the beam splitter to have the same amount of whitelight counts as the probe when it reaches the sample. The probe and reference run parallel along a vibration controlled table until reaching another off-axis parabolic mirror ( $f = 15.24$  cm) to focus them at sample position. They are not overlapped, but they are as close as possible to each other to allow for the best results. The purpose of the probe beam is to monitor the perturbation in the sample created by the pump beam, while the reference beam passes through an unperturbed part of the sample to act as a reference in the calculations. After the sample, lenses are used to collimate and then refocus the beams on the entrance slit of a spectrograph.

The 420 nm pump beam out of the OPA is measured to travel the same distance to the sample as that of the probe and reference beams so that the beams can be temporally overlapped. The mirrors it encounters are chosen to provide the best reflection at 420 nm, while the mirrors for the whitelight must be able to reflect a broader spectrum of light. The pump first passes through a telescope made up of two quartz lenses (concave:  $f = -50$  nm; convex:  $f = 150$  nm) in order to decrease the beam size and to collimate it. The probe beam then passes through an optical delay stage which contains two perpendicular mounted mirrors on a computer-controlled horizontal translation stage.<sup>77</sup> This enables one to change the time delay between the pump and probe up to 800 ps during experimentation. After the delay stage, the pump beam passes a mechanical chopper wheel with repetition rate of 8.4 Hz which allows for data

collection with the pump on (not blocked) and off (blocked). Then the pump beam hits the same parabolic mirror ( $f = 15.24$  cm) as the probe and reference, and is focused so that it completely overlaps the probe beam. The diameter of the pump was measured using a “razor-blade edge” technique to be 276 microns.<sup>77</sup>

The film sample is placed film side facing towards the incoming beam at the focus of the parabolic mirror. Any group velocity dispersion from the glass is corrected for during data analysis using a homemade Labview® program. After alignment, the pump and probe beams are now overlapped on the part of the film to be tested, with the reference beam right below (Figure 3-5). It is essential that the probe beam is smaller than the pump beam ( $d = 276$   $\mu\text{m}$ ) and that their overlap is optimized to make sure every molecule in the probed volume is excited. Partial overlap will give a low signal to noise ratio from a much weaker change in the collected signals.

### **Detection System**

After the sample, the pump beam is blocked with a beam stopper, and the transmission through the sample of both the probe and reference beams are collimated by a lens, then focused by another lens onto a 150  $\mu\text{m}$  entrance slit of an Andor iStar® Shamrock spectrograph. The beams arrive at two different heights. After an internal grating with line density of 300 lines/mm disperses the wavelengths, they are then independently detected on different rows of pixels by a Charge-Coupled Device (CCD) camera and read by Andor iStar® and LabView® programs. The CCD is a silicon-based semiconductor chip bearing 256 rows and 1024 columns of photo-sensors (pixels). The whitelight beams cover about 13 rows each (which are integrated for data collection), and are separated by at least 50 rows between them. The grating angle in the monochromator of the Shamrock can be changed to collect the desired wavelengths

of light, and is chosen here to show the spectral coverage from 350.49 to 631.21 nm, because the range of counts generated from the CaF<sub>2</sub> window only show measurable counts between ~350 nm and ~600 nm, with the highest counts around 450 nm.

Averaging was implemented to improve the signal to noise ratio. For each experiment, unless otherwise noted, an average of 80 points at each time-step was taken. Then, at least 10 experiments were run for each study, and the best 10 experiments were taken and averaged. About 50 time steps were used to show the entire range from -50 ps to 800 ps (after ~200 ps there was little signal), with time steps much closer to each other at times just following excitation at time zero. If significant degradation of the magnitude of the data was seen from experiment to experiment, the film was moved horizontally perpendicular to the beam in order to hit a fresh spot.

### **Modifications**

The film sample is secured on a homemade three-dimensional-adjustable translation stage for proper alignment. A circularly rotating stage attached to this translation stage is positioned so that film samples can be taped to it. Rotation of the films benefits the data collection in three ways: 1) it prevents the film from burning because the slide will be moving and the focus will hit different parts, 2) it provides an average for the entire film, which is useful because often the film surfaces may not be the exact same thickness throughout, and 3) it helps assure that each shot is exciting a new part of the film which starts in the ground state.

The range of wavelengths collected by the CCD after the monochromator's grating dispersion are from ~350 nm to ~630 nm, which covers the bleach signal at 420 nm and possible stimulated emission peak found at 525 nm. Furthermore, emission from the TiO<sub>2</sub> quencher may also be seen from about 500 nm up to the longer

wavelength edge of the detectable spectrum;<sup>42</sup> therefore, these wavelengths are also monitored for any stimulated emission which may result.

Lastly, numerical corrections to the TA data, including that for chirp, (which is a consequence of the temporal distribution of the different wavelengths of the whitelight, which causes the signal to appear earlier at shorter wavelengths than longer ones due to the beams passing through materials other than vacuum,) are implemented using a homemade LabView® program.<sup>50,28</sup> An instrument response function (IRF) was found in previous solution studies,<sup>77</sup> but could not be done for films because there is no solvent to test for coherent artifacts. Based on that previous work, it is assumed that the IRF is somewhere between 100 and 250 fs. Finally, a calculation of Equation 3-3 to convert change in transmission to change in absorption was done to all the TA data.

Fluences are defined as energy per unit area. For the pump diameter of 276 microns and energies measured using an Ophir® power meter (at 420 nm) of 50 nJ, 30 nJ, 15 nJ, and 7 nJ at the sample position, one calculates fluences of 84  $\mu\text{J cm}^{-2}$ , 50  $\mu\text{J cm}^{-2}$ , 25  $\mu\text{J cm}^{-2}$ , and 12  $\mu\text{J cm}^{-2}$ , respectively. These fluences may be lower than expected because of reflection losses in some of the optical components, and because on certain days full power from the Spitfire could not be obtained. Because of the 1 kHz repetition rate, the irradiances, in units of power/area, would simply be 84  $\text{mW cm}^{-2}$ , 50  $\text{mW cm}^{-2}$ , 25  $\text{mW cm}^{-2}$ , and 12  $\text{mW cm}^{-2}$ , respectively.

### **Atomic Force Microscopy**

Measurements done using Atomic Force Microscopy (AFM) were employed in order to elucidate the film surface structure. It is important in these studies that a uniformly rough surface is obtained, otherwise the TA results would not be reproducible. During the TA data collection, the rotating sample stage was added in order to average

the film absorption, so if the film only contains minor impurities or changes in roughness, those would not greatly affect data results.

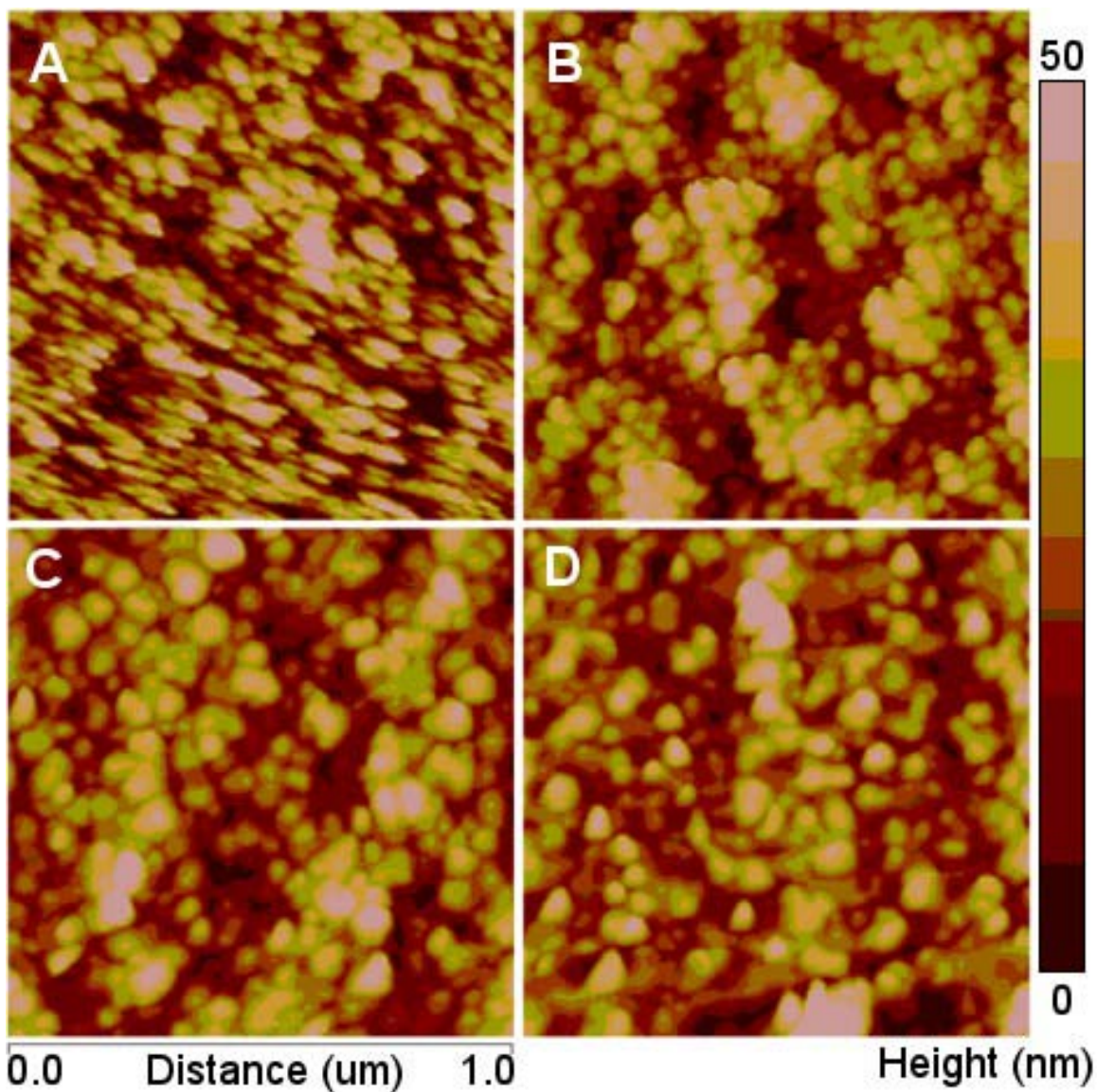


Figure 3-6. AFM image for A) 5, B) 10, C) 20, and D) 30 Bilayers. Darker areas are shallow regions, while the bright pink areas are the tops of TiO<sub>2</sub> nanoparticle clusters. It is not possible to clearly distinguish the polymer layers on the films.

Figure 3-6 shows AFM images of four films, one of each of 5, 10, 20, and 30 bilayers of PDDA/PPE-SO<sub>3</sub>. They were taken after a week of the initial fabrication. The 5 bilayer film appears “stretched” from side to side, which is not necessarily bad for the

TA studies, but is likely due to the doctor-blading process which drags titania material across the slide. In general, the size of the clusters and film roughness stay the same, or possibly a very slight trend can be seen going from fewer to greater number of bilayers, in which more bilayers equals larger clusters. In the bottom of picture “D,” the top half of a large cluster can be seen as a bright pink spot, thus showing that the largest clusters are found with the highest number (30) of bilayers.

It is believed that overall, the titanium dioxide nanoparticles make up the majority of the film thickness and structure, but through aggregation and a simple accumulation of material, the additional bilayers appear as a small, not quite conclusively visible increase in the thickness throughout the film structure.<sup>65</sup> This is because the CPE bilayers individually account for only tens of nanometers on the overall micron thickness made from the 20 nm TiO<sub>2</sub> nanoparticles,

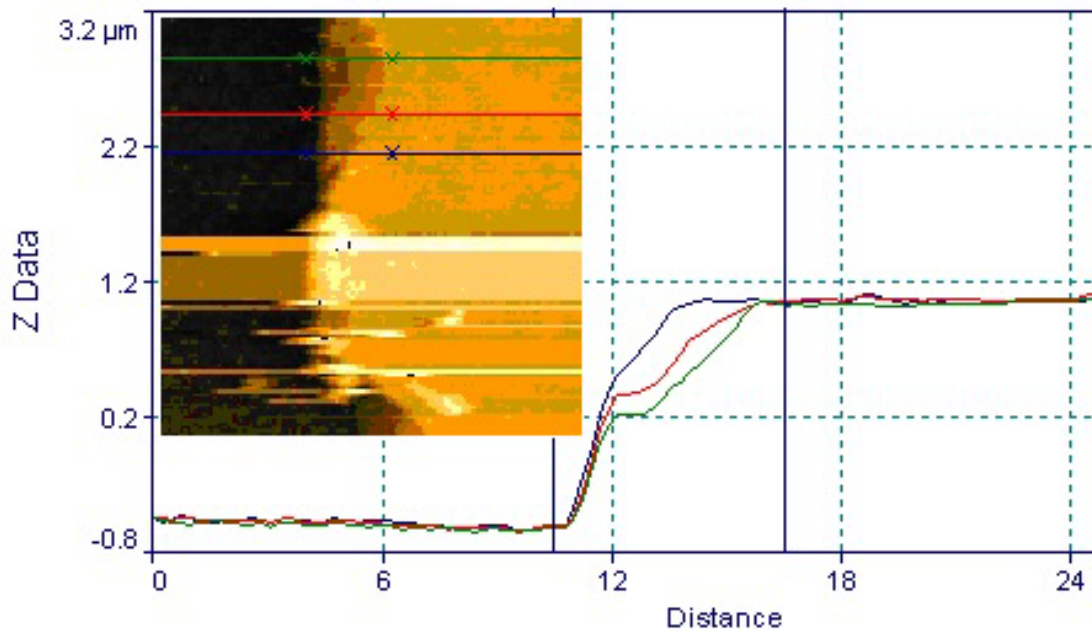


Figure 3-7. AFM “step-height” measurement on 10 bilayer film, taken at three different spots on the film, indicated by the three lines. All lines give ~1.60  $\mu\text{m}$  as the height between the glass and the surface.

A “scratch” method, using the side of a razor blade to remove the film down to the glass, was employed, and then the AFM was run in step-height calculation mode. It required a couple trials to find a good spot, which was assisted by blowing off of residue from the scratch. After some simple analysis using the provided AFM software, Figure 3-7 was obtained.

In Figure 3-7, the dark area represents the scratched away part, showing the glass surface, while the orange part is the remaining film. From a calculation of the difference in the z value (height), a film thickness of a little more than 1.60 microns was found. This matches well with the literature, where titania coatings were made using a few microns as the thickness.<sup>65,66,68</sup>

## CHAPTER 4 TRANSIENT ABSORPTION RESULTS AND ANALYSIS

This chapter outlines the results of the transient absorption experiments performed on the PDDA<sup>+</sup>/PPE-SO<sub>3</sub><sup>-</sup> bilayer titania films.

### **Transient Absorption Results for 30 Bilayer Film**

In the first experiment, the 30 bilayer film was excited with 50 nJ of energy measured at 420 nm at the sample position. This was the maximum energy that could be attained, so all other scans which required a change in energy were done by reducing the energy using a waveplate placed inside the OPA. A complete three-dimensional representation using Matlab® software on the data is found in Figure 4-1, followed by two two-dimensional cross-sectional plots in Figures 4-2 and 4-3, made by selecting either times or wavelengths. The TA data were collected from a range of -20 ps to 200 ps, and a wavelength range based on the probe's whitelight spectrum which gave usable counts between 350 and 600 nm.

The first thing to note about these data plots is that they show a narrow peak at ~420 nm which is simply pump scatter. In Figure 4-1, this was removed by setting absorption values arbitrarily to zero, while in Figure 4-2, the full magnitude of this scatter is seen. Despite setting up numerous beam blockers, this could not be fully eliminated. Fortunately, it does not hinder the analysis of wavelengths outside of the narrow range of about 414 to 422 nm.

### **Bleach**

Ignoring those scatter points, one sees a decrease in absorption from about 380 to 460 nm due to the bleach signal. This negative signal, centered at the 420 nm peak of the ground state absorption, corresponds to the population of chromophores being

unable to continue to absorb at those wavelengths because many are in the first excited singlet state, and if there is a state with energy difference  $\Delta E = h\nu$  above the singlet to which the population can further absorb, the signal is not strong enough to detect it.

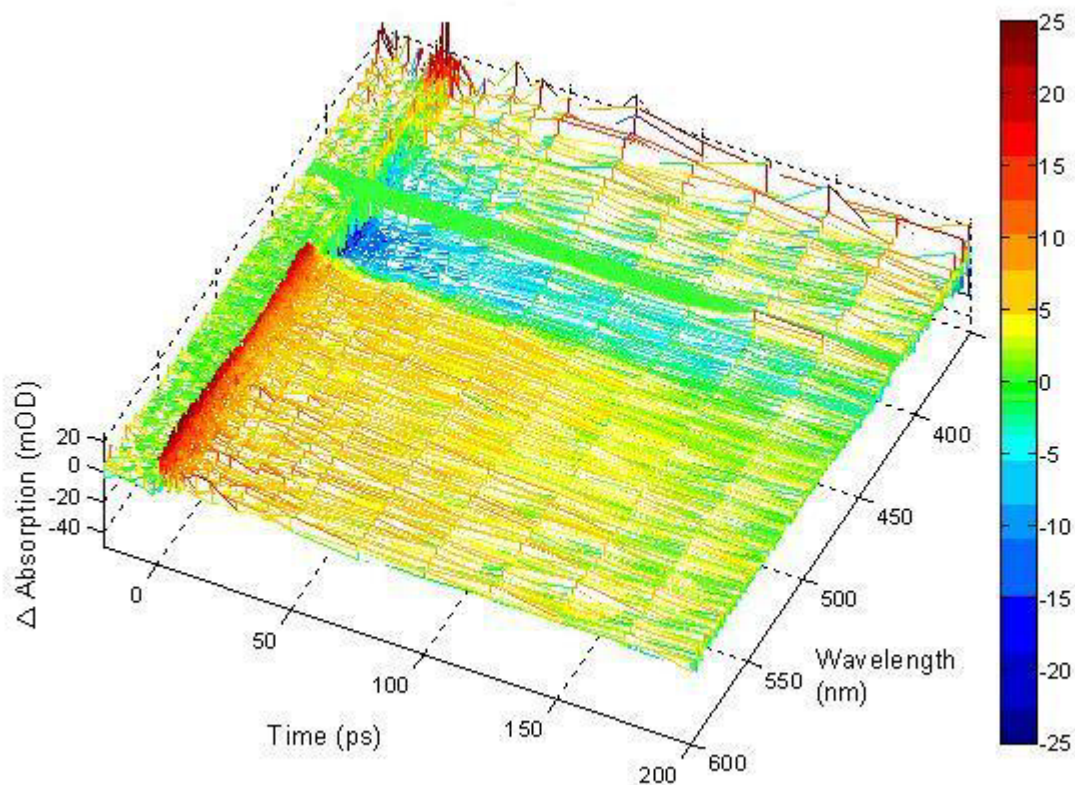


Figure 4-1. Complete TA data for 30 BL film excited with 50 nJ pump energy. The positive absorption (in red) can be seen to rise sharply at 0 ps, and then decrease in intensity out towards 200 ps. The negative absorption signal (in blue) is also strongest right after 0 ps, and then becomes less negative as it approaches 200 ps. The pump scatter was removed around 420 nm wavelengths, and is seen as an arbitrary green band. The signals at wavelengths lower than 400 nm is noisy and is not assumed real.

Upon closer inspection of Figure 4-2, the bleach signal can be seen not to match the steady state absorption because of the narrowing on the shorter wavelength side (380 to 410 nm) and possible narrowing on longer wavelength side, around 450 to 460 nm. Both may be due to a PIA band of the CPE being superimposed with the bleach

signal, thus giving a summation of two opposite magnitude absorption signals in the spectrum. The shorter wavelength narrowing may also include contribution due to absorption from the TiO<sub>2</sub> or glass. Thus, the bleach signal contribution, because it is not a similar shape to the linear absorption band in Figure 3-1 (included normalized to 57 mOD in Figure 4-2), may also contain another process below 410 nm and above 450 nm, causing the total TA signal to appear less negative. To separate these signals, further computational methods, outside the scope of this paper, would be required.

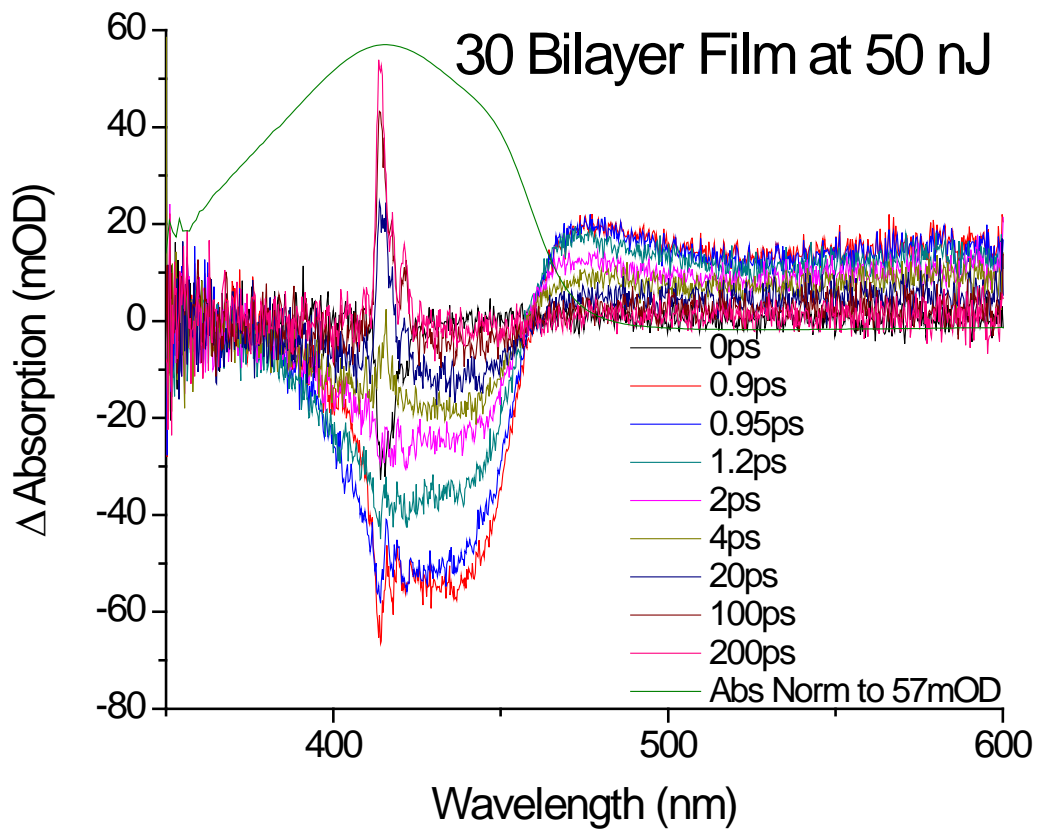


Figure 4-2. 30 BL film excited with 50 nJ pump energy, plotted selecting time cross-sections to show the dynamics. Pump scatter is seen around 420 nm. Ignoring this, a broad negative absorption bleach band is seen between 380 and 460 nm, while a PIA positive absorption signal, with possible stimulated emission contribution near 525 nm, is seen between 460 and 600 nm. The steady state absorption normalized to 57 mOD is shown for comparison.

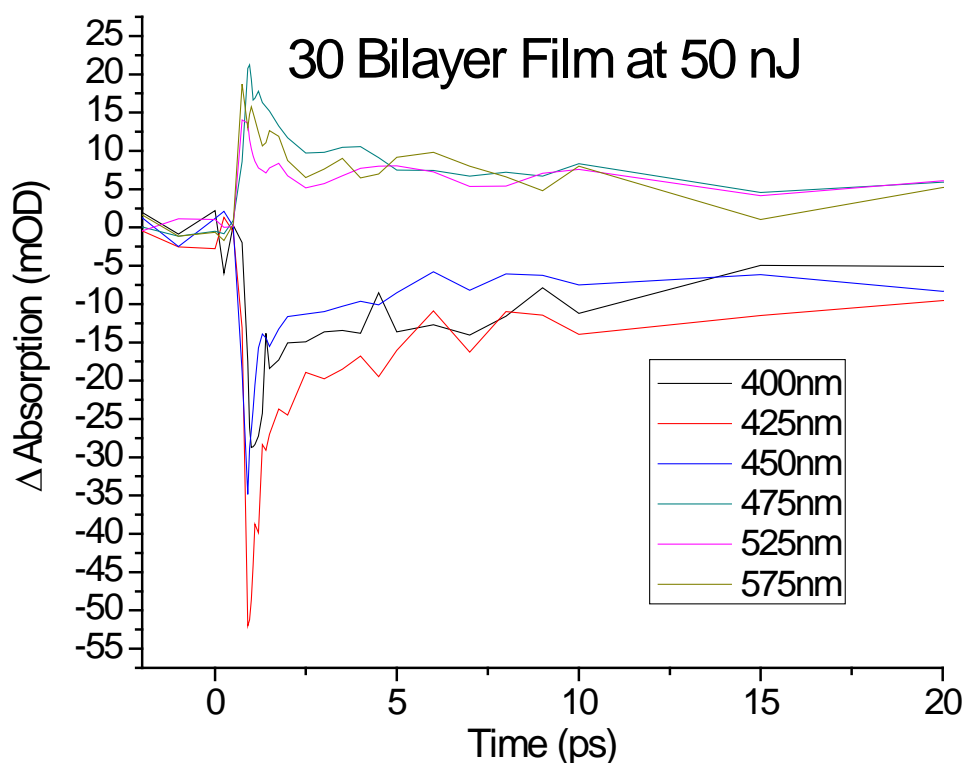


Figure 4-3. 30 bilayer film excited with 50 nJ pump energy, plotted selecting wavelength cross-sections to show the decays. At 400, 425, and 450 nm, the bleach signal decays from negative absorption, while at the 475, 525, and 575 nm, the PIA signal decays with a weaker and positive signal.

### Photo-induced Absorption (PIA)

At 475 nm, after initial excitation (0.9 ps on the plot), the positive absorption signal decays in a few picoseconds in Figure 4-2. To determine what causes this PIA, it is necessary to list the possibilities. It could be due to: 1) absorption from the titania layer after electron injection occurs<sup>67</sup> (before electron injection occurs the TiO<sub>2</sub> absorbs in the near-UV region), 2) absorption from the PPE-SO<sub>3</sub><sup>+</sup> after electron injection occurs, or 3) absorption of light by the singlet state of PPE-SO<sub>3</sub><sup>-</sup> into a higher energy excited state. The first thing to note is that the titania layer is ruled out from causing the strong 475 nm signal because literature value show TiO<sub>2</sub><sup>-</sup> absorption to be broad and centered around

620 nm.<sup>65-67</sup> Second, molecules similar to the cationic PPE-SO<sub>3</sub><sup>+</sup> have been studied, and they also absorb above 600 nm,<sup>18</sup> out of the range of this test, so that can not be the source of PIA. Therefore, it can be concluded that the observed photo-induced absorption must be due to PPE-SO<sub>3</sub> excited state absorption.

The broadness of this absorption is convoluted with the bleach on the shorter wavelengths around 460 nm, and perhaps some stimulated emission centered at 525 nm which essentially subtracts from the absorption signal seen.

### **Stimulated Emission (SE)**

Although the signal in Figure 4-2 shows positive absorption (PIA) at wavelengths above 460 nm after pump excitation, the signal is *less* positive around 525 nm. Because this corresponds to the peak in the fluorescence signal of PPE-SO<sub>3</sub>, stimulated emission from PPE-SO<sub>3</sub> is the most likely cause. The broad shape of the dip also points to a subtraction in detected absorption from the broad aggregated emission from PPE-SO<sub>3</sub>. An additional contribution may be due to the titania stimulated emission (after electron acceptance). To determine which contributes to the signal, the shapes need to be compared to that of the TA data. This is done in Figure 4-4, where Figure 4-2 is adapted to show the 30 bilayers TA data with the fluorescence of TiO<sub>2</sub> and PPE-SO<sub>3</sub> overlapped and normalized to 32 mOD.

Subsequently, the first interpretation of the signal at 525 nm is as a combination of positive absorption PIA of the singlet state PPE-SO<sub>3</sub>, plus a negative signal due to stimulated emission from the excited state of PPE-SO<sub>3</sub>. An alternate interpretation of the signal above 460 nm is that of two PIAs with no stimulated emission necessary. The first PIA (475 nm) would be due to the excited state absorption and the second (575 nm) would be due to the negatively charged titania. As mentioned earlier, TiO<sub>2</sub><sup>-</sup>

absorbs in a broad, featureless shape between 400 to 800 nm.<sup>67</sup> Thus, it could be that that absorption is partially hidden in the spectra, and only detected alone (not as a combination of signals) at wavelengths greater than 525 nm. A different interpretation still is that of PIA of PPE-SO<sub>3</sub> with TiO<sub>2</sub> SE, but based on the lack of shape similarity near 520 nm in Figure 4-4, this is least likely. Future tests are necessary to visualize the PIA above 600 nm to decide for certain what the cause is. Probing higher wavelengths would additionally be beneficial in elucidating the dynamics of PPE-SO<sub>3</sub><sup>+</sup>.

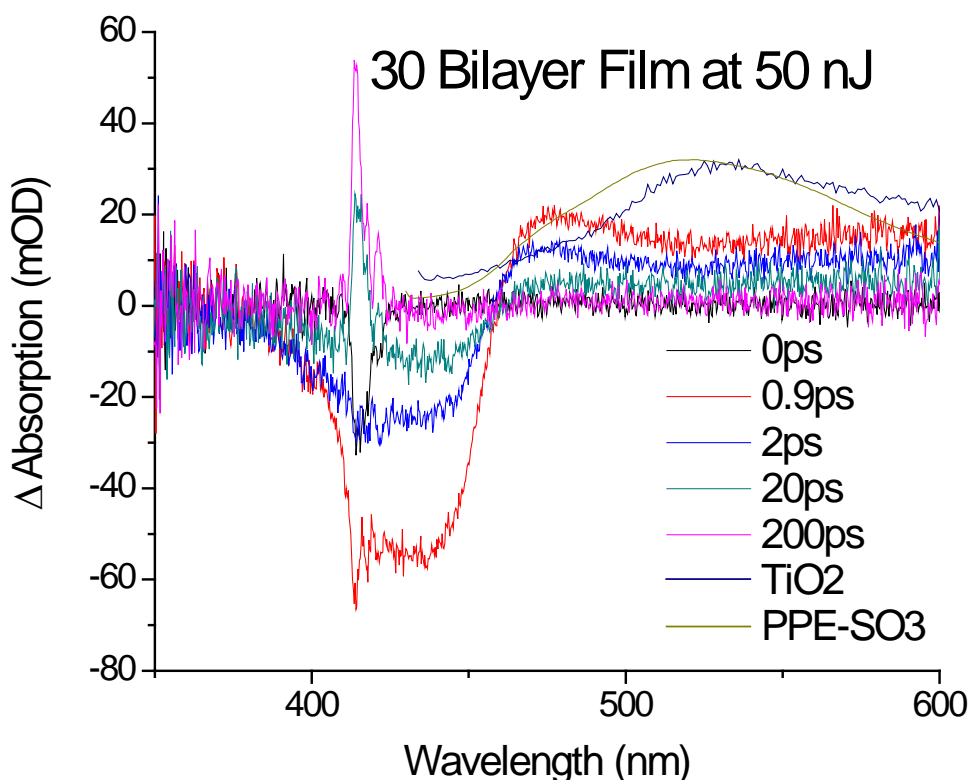


Figure 4-4. 30 BL film excited with 50 nJ pump energy, plotted selecting time cross-sections to show the dynamics. In this plot, the curves for titania and PPE-SO<sub>3</sub> fluorescence are added to try to account for stimulated emission. Both are normalized to 32 mOD. They are close in shape, but SE from PPE-SO<sub>3</sub> is believed to be the main cause.

## Assigning Bands

The initial absorption of 425 nm light by PPE-SO<sub>3</sub> from the ground state to the first electronic excited state can be represented by a Perrin-Jablonski diagram, as shown in Figure 4-5. Here, PIA excites the first excited singlet state of PPE-SO<sub>3</sub> to a higher energy excited state through the absorption of 475 nm light. Within 10<sup>-12</sup> s to 10<sup>-10</sup> s after both of these absorptions, vibrational relaxation to the lowest vibrational level of the electronic excited state occurs,<sup>50</sup> and in the case of the first singlet, stimulated emission from it (or one of the aggregated states to which the energy moved) to one of the ground state's vibrational levels can be detected at 525 nm. From the TA data, it can not be concluded definitely if other states, whether a triplet of PPE-SO<sub>3</sub> or simply titania, are present, but SE from the titania is not completely ruled out because higher wavelength dynamics are not yet known. Triplets however are much less probable because their characteristic longer lifetimes were not seen.

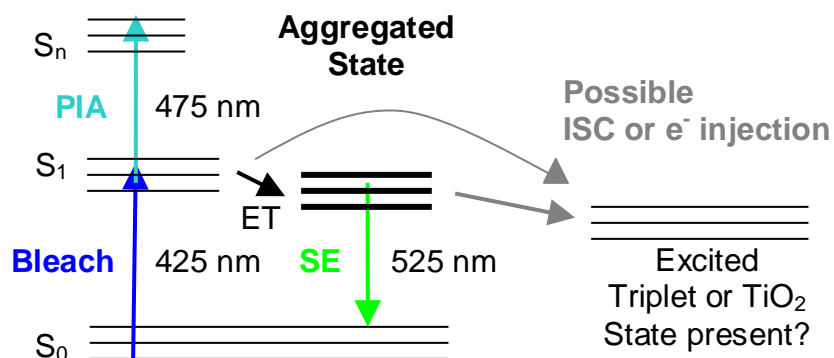


Figure 4-5. Spectral band assignment from TA data using a Perrin-Jablonski diagram. The bleach occurs at 420 nm, the photo-induced absorption at 475 nm, and the stimulated emission at 525 nm. It is not clear from data collected which other states and processes are present.

## Exciton-Exciton Annihilation

Exciton motion and diffusion determination can give important information about the nanoscale structure of polymer films. However, no universal method has been determined to calculate fully the diffusion process, although many suggestions, like by adding quenching centers, testing with a metal present, and depolarization experiments, have been made.<sup>61-65</sup> One method to determine exciton diffusion is through studies of the excitation energy dependence on exciton-exciton annihilation rates. Exciton-exciton annihilation (EEA) occurs when two excitons diffuse to within close proximity of each other, known as an “annihilation radius.”<sup>80</sup> Once there, the two excitons can interact via dipole-dipole processes, causing the energy of one exciton to be transferred to the other.<sup>81</sup> The exciton in the higher excited state quickly relaxes non-radiatively back to the lowest excited state. The net result of this bimolecular process is the loss of one exciton to heat.<sup>70,80-81</sup>

Because there are fewer excitons after EEA because some returned to the ground state, it is expected that the greater the extent of EEA, the shorter the lifetime of time-resolved signals (such as bleach) will be. Bleach signals are seen in TA experiments because of a reduction of the ground state population, so as EEA occurs, the ground state population will return more quickly, and a faster decay of the bleach signal should be seen. By solving exciton rate equations and using TA data, Gulbinas et al. have been able to use time-resolved signals measured for different fluences to calculate exciton diffusion values.<sup>62</sup> These equations and PPE-SO<sub>3</sub> film TA data are presented in the next few sections to calculate annihilation rate constants and determine preliminary values for exciton diffusion in a similar manner.

It is important to know about the diffusion of excitons generated by photons in thin films because it is this process which contributes to photocurrent, should the films used in photovoltaic devices, by allowing excitons generated by photo-excitation in the bulk of the polymer to diffuse to the polymer-acceptor interface where electron-hole separation occurs. The higher the average distance traveled during their "random walk,"<sup>29</sup> the higher the number of neutral excitons which will reach the bulk interface with titania and be able to be cleaved into unbound electrons and holes.

### Exciton Density Calculation

In order for EEA to occur, exciton densities of a sufficiently high value must be achieved. In the literature, densities of at least  $10^{17} \text{ cm}^{-3}$  are usually needed.<sup>80-81</sup> Therefore, in order to see if EEA is taking place in these PPE-SO<sub>3</sub> films, the exciton density needs to be calculated. First, using the typical density of polymer films<sup>72</sup> of  $1 \text{ g cm}^{-3}$  and chromophore mass, the chromophore density ( $\rho$ ) can be obtained:

$$\rho = \frac{1\text{g}}{1\text{cm}^3} \left[ \frac{1\text{molPRU}}{474.51\text{g}} \right] \left[ \frac{1\text{chromophore}}{5\text{PRU}} \right] \left[ \frac{6.022 \times 10^{23}}{1\text{mole}} \right] \approx 2.54 \times 10^{20} \text{ cm}^{-3} \quad (4-1)$$

The exciton density can be calculated based on the number of photons absorbed. One can use  $v = c/\lambda$  and  $E = hv$  to determine that one photon of 420 nm wavelength has an energy of about  $4.73 \times 10^{-19} \text{ J}$ . In 50 nJ, the highest excitation energy used, there are then  $1.06 \times 10^{11}$  photons.

Furthermore, using  $A = \log(I_0/I)$  where "A" is absorbance and " $I_0$ " and "I" are intensity entering and leaving the excitation volume, one can determine that 67.8% of photons are absorbed based on  $A = 0.492$  (background subtracted) at 420 nm. 67.8% of  $1.06 \times 10^{11}$  photons equals  $7.19 \times 10^{10}$  photons. This is how many photons were absorbed per  $\text{cm}^3$  for 50 nJ energy excitation. From the AFM step-height measurement,

the thickness of the films, including titania, is about 1.60 microns; however, of that volume, only about a 41 nm thickness contains PPE-SO<sub>3</sub> interwoven amid the titania scaffold, so that can be assumed to be the absorption layer thickness (see Table 2-1). From “razor-blade” experiments in the lab which determined the focused pump beam diameter to be 276 microns, one can approximate the active cylindrical volume as:

$$V = [\pi r^2] [t] = [\pi(138)^2 \mu m^2] [41 nm] = 2.45 \times 10^3 \mu m^3 = 2.45 \times 10^{-9} cm^3 \quad (4-2)$$

The final step to calculate the exciton density is to take the number of photons absorbed by PPE-SO<sub>3</sub> (each of which became an exciton) and divide by the active volume, which for 50 nJ excitation gives  $2.93 \times 10^{19} cm^{-3}$ . For 30 nJ and 15 nJ excitation, the exciton density values are  $1.76 \times 10^{19} cm^{-3}$  and  $8.78 \times 10^{18} cm^{-3}$ , respectively. All of these numbers are above the minimum  $10^{17} cm^{-3}$  density value expected for EEA to occur; thus, it is concluded that EEA occurs under the experimental conditions presented here.

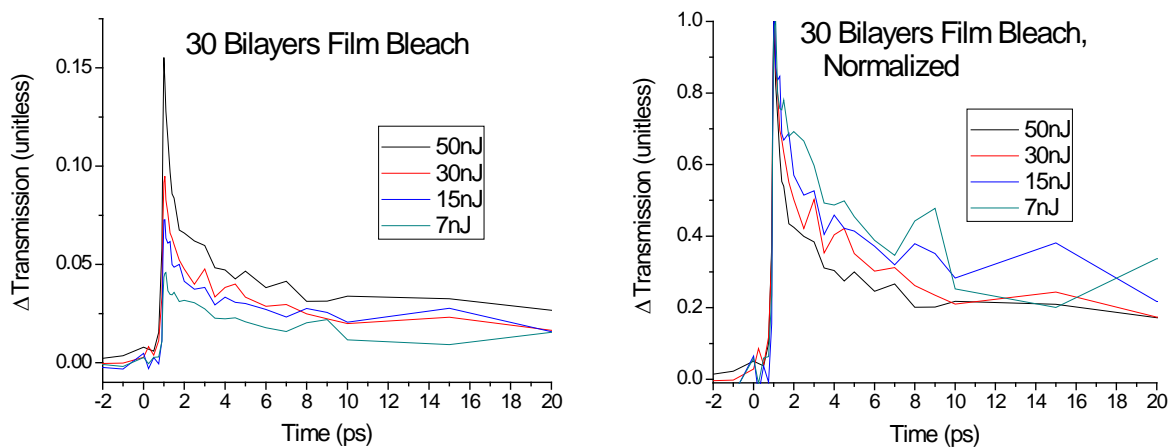


Figure 4-6. 30 bilayer film bleach signal ( $\lambda_{excitation} = 420 nm, \lambda_{detection} = 427 nm$ ) from four different excitation energies, 7, 15, 30, and 50 nJ. Each curve is the average of 10 experiments, 80 points averaged per time-step, per experiment. These data are raw and uncorrected to show the EEA in the first few picoseconds. The graph on the right is normalized data, showing 50 nJ decays fastest.

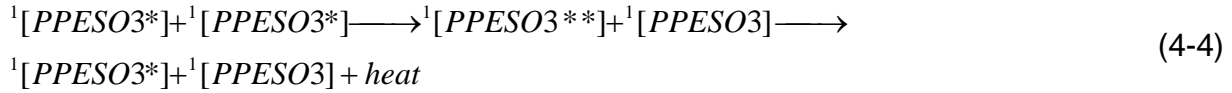
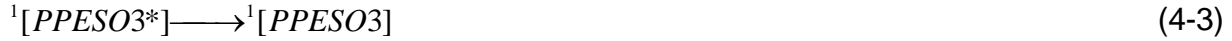
To further show that EEA is happening, Figure 4-6 is presented to show energy dependence on the EEA of the bleach signal for the 30 bilayer film. The data are not corrected for chirp or converted to change in absorption yet because the purpose here is just to show the energy dependence. The presence of a fast decay component appears upon increased excitation, as seen in the sharper decay for the 50 nJ energy excitation in the first few picoseconds after excitation. The lower energy excitations show a slower decay indicating weaker EEA; this is also shown in the graph on the right of Figure 4-6, which simply normalized the data on the left.

Gulbinas et al. showed that EEA in films occur at fluences orders of magnitude lower than for solutions.<sup>62</sup> Their polymer films, methyl-substituted polyparaphenylene (m-LPPP), begin to show EEA at fluences of  $30 \mu\text{J cm}^{-2}$ . The fluences, calculated from the excitation energies and spot size radius of  $138 \mu\text{m}$ , used in the PPE-SO<sub>3</sub> films are:  $84 \mu\text{J cm}^{-2}$  (50 nJ),  $50 \mu\text{J cm}^{-2}$  (30 nJ),  $25 \mu\text{J cm}^{-2}$  (15 nJ), and  $12 \mu\text{J cm}^{-2}$  (7 nJ). So besides the visual appearance of EEA at the first few picoseconds in Figure 4-6, the fluences calculated show that at least for the two highest excitations, there should be EEA. Unfortunately, higher fluences could not be obtained during these tests, but hopefully future tests can be done using higher values to verify the results found here.

### **Kinetics**

The 30 BL films (and 20 BL films, not shown) were excited at different energies to determine the extent of exciton diffusion through annihilation studies. To understand how this is done, it is first necessary to examine the kinetic equations describing the pathways of exciton relaxation. Equation 4-3 shows one of the possible deactivations, while Equation 4-4 models the annihilation process. There are numerous pathways for the exciton to decay, including PIA, stimulated and spontaneous emission, internal

conversion, intersystem crossing, and quenching by the titania layer. All of these deactivation pathways are accumulated in a linear rate constant,  $k$ , which separate them from the annihilation rate constant  $\gamma$ .<sup>56,80</sup>



Exciton-exciton annihilation can be expressed as Equation 4-5.<sup>62,80</sup>

$$\frac{d[n^*]}{dt} = -k[n^*] - \gamma[n^*]^2 \quad (4-5)$$

where  $[n^*]$  is the exciton density. The annihilation term has an exciton density squared dependence because EEA obviously requires two excitons to interact. An initial pumping term is not included in Equation 4-5, but it is known that pumping to create excitons occurs at the initial time. The goal is to isolate and solve for  $\gamma$ , so first both sides of Equation 4-5 are divided by  $[n^*]$ . Then the exciton relaxation rate,  $K$ , is defined as in Equation 4-6:

$$K = \frac{1}{[n^*]} \frac{d[n^*]}{dt} \quad (4-6)$$

which leads to an annihilation rate constant as in Equation 4-7:

$$\gamma = -\frac{(K + k)}{[n^*]} \quad (4-7)$$

Although  $[n^*]$ , the exciton density, has time dependence, the rate constants  $k$  and  $\gamma$ , from basic kinetic considerations, are assumed to be time independent. When necessary, the exciton density is thus taken as the value at the initial time, and for  $K$  calculations, is incorporated into the relative derivative which is obtained from data.

At this point, K (from smoothing the bleach signal decay and differentiating) and  $[n^*]$  can be obtained from the data and measurements, but k is still unknown, unless one determines additional parameters by comparing two excitation energies, thus isolating the k term. It was seen in Figure 4-6 that at different excitation energies the bleach decay rates are different at short timescales, so this means different K values can be obtained. Putting together two equations at different energies, noted with subscripts 1 and 2, one can get Equations 4-8 and 4-9.<sup>62</sup>

$$\gamma = -\frac{K_1 - K_2}{[n_1^*] - [n_2^*]} \quad (4-8)$$

$$k = -\frac{K_1[n_2^*] - K_2[n_1^*]}{[n_1^*] - [n_2^*]} \quad (4-9)$$

### Data Fitting to Find Rate Constants

Now the TA data are analyzed for different fluences to give values for K, which will then be used along with the exciton density to give an estimate of the annihilation rate coefficient. Appropriately, Figures 4-7, 4-8, and 4-9 show the (10 experiment averaged) data obtained during TA data collection (at bleach wavelength) for the 30 bilayer film excited with 50, 30, and 15 nJ pump excitation energy, respectively. The 50 and 30 nJ energies data was plotted for 425 nm detection, while the 15 nJ data was plotted using 427 nm because of a clearer signal seen at that wavelength. A “three point adjacent averaging” smoothing was implemented in order better evaluate the derivative of the data. This was done using the Origin® software program. Residuals for the smoothings are also plotted as insets in these figures to show that the deviation from the actual data is uniformly random, so the smoothing can be trusted.

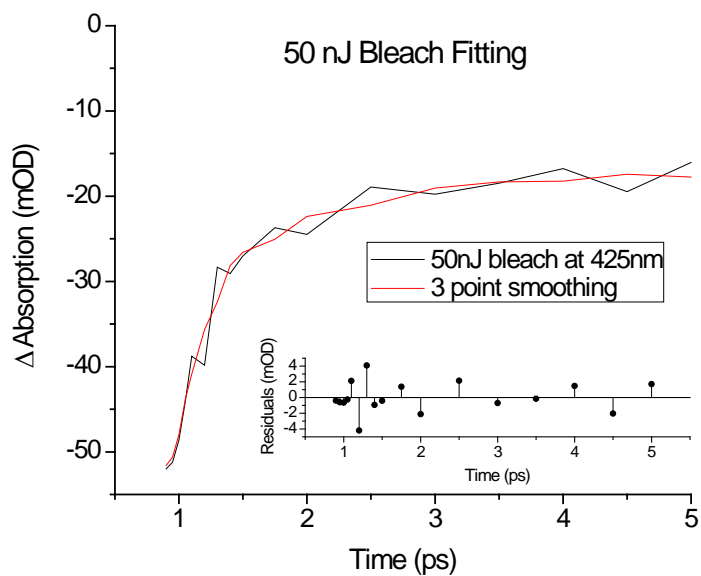


Figure 4-7. 30 bilayers film excited with 50 nJ energy from 420 nm pump beam. Detected at 425 nm. “3 point adjacent averaging” smoothing is shown as the red line. Residuals between data and smoothing are shown in the inset.

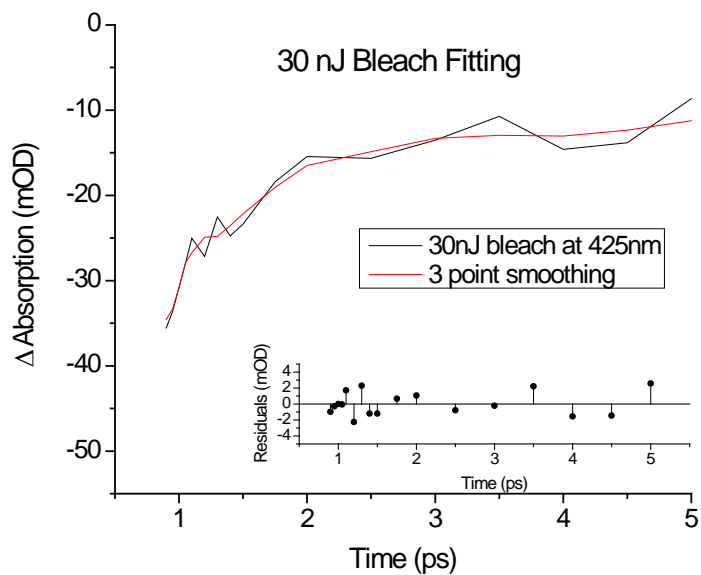


Figure 4-8. 30 bilayer film excited with 30 nJ energy from 420 nm pump beam. Detected at 425 nm. “3 point adjacent averaging” smoothing is shown as the red line. Residuals between data and smoothing are shown in the inset.

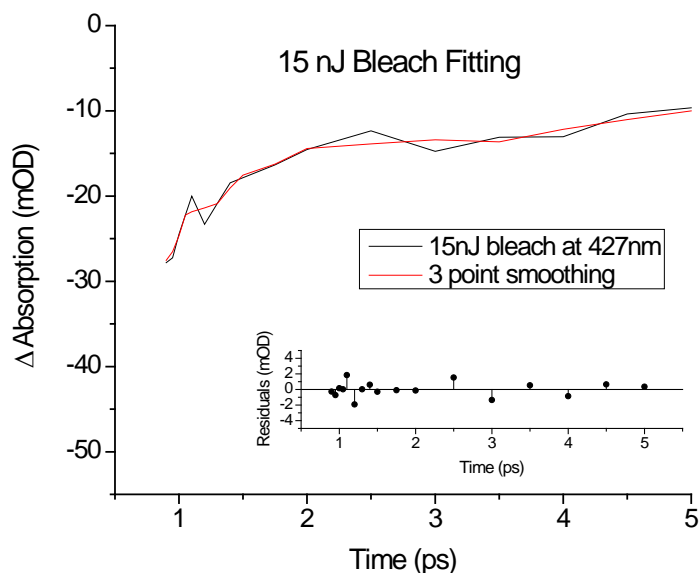


Figure 4-9. 30 bilayer film excited with 15 nJ energy from 420 nm pump beam. Detected at 427 nm. “3 point adjacent averaging” smoothing is shown as the red line. Residuals between data and smoothing are shown in the inset.

Once the simple smoothings were obtained for each excitation energy, the derivatives were taken in order to give values for  $K$ , the exciton relaxation rate. These are plotted in Figure 4-10. The derivatives are highest right after the initial excitation as expected. It is clear that the relative derivatives, which are taken as the  $K$  values according to Equation 4-6, vary over time, but the relatively large errors present a significant drawback in evaluating the numerator in Equation 4-8. Because the assumption is being made that the annihilation rate is time independent during the first few picoseconds (based on EEA film work by Gulbinas et al.),<sup>62</sup> the best that can be done is to choose  $K$  values at a point in time at which the derivatives show the least amount of error. The point chosen is 0.6 ps after excitation. At this value, the derivatives in Figure 4-10 do not show the large error seen at earlier time, show a clear difference in values as opposed to later times, and align such that the higher excitation

energy data derivatives yield a higher derivative and K value. The last reason makes sense because the excitation with higher energy (50 nJ) should create more excitons, each of which should “see” more excitons than the system with fewer excitons created (15 nJ). The K values 0.6 ps after excitation are:  $K_{50} = 17.821 \times 10^{12} \text{ s}^{-1}$ ,  $K_{30} = 13.045 \times 10^{12} \text{ s}^{-1}$ , and  $K_{15} = 10.096 \times 10^{12} \text{ s}^{-1}$ .

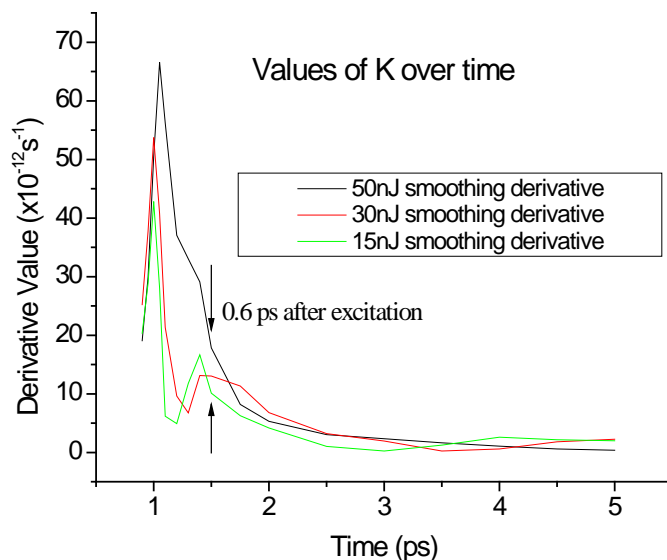


Figure 4-10. K values over time, for excitation energies of 50 nJ, 30 nJ, and 15 nJ.

Equation 4-8 can now be evaluated. The difference in K values gives the numerator, and the difference in exciton densities gives the denominator. Table 4-1 shows these values calculated for each of the three pairs of excitations. The absolute value of the annihilation rate constant is estimated from Equation 4-8, but should be noted to have high error. The  $\gamma$  values are similar to each other, and the average of them is  $3.73 \times 10^{-7} \text{ cm}^3 \text{ s}^{-1}$ . The linear relaxation rate from Equation 4-9 is not calculated because it is not needed in diffusion coefficient calculations in the next section, and because it is expected to be unreliable due to the noise in the TA data.

Table 4-1. Calculation of annihilation rate constant for 30 bilayer film.

Excitation Pair	$K_1-K_2$	$n_1^*-n_2^*$	$\gamma$
50 & 30 nJ	$4.78 \times 10^{12} \text{ s}^{-1}$	$1.17 \times 10^{19} \text{ cm}^{-3}$	$4.09 \times 10^{-7} \text{ cm}^3 \text{ s}^{-1}$
50 & 15 nJ	$7.73 \times 10^{12} \text{ s}^{-1}$	$2.05 \times 10^{19} \text{ cm}^{-3}$	$3.77 \times 10^{-7} \text{ cm}^3 \text{ s}^{-1}$
30 & 15 nJ	$2.95 \times 10^{12} \text{ s}^{-1}$	$8.82 \times 10^{18} \text{ cm}^{-3}$	$3.34 \times 10^{-7} \text{ cm}^3 \text{ s}^{-1}$

### Exciton Diffusion Length Calculations

The 50 nJ and 15 nJ excitation energies were chosen because they were the farthest stable energies apart which could be obtained, considering the irradiated area, both energies would result in fluence values that should still produce annihilation, and their difference should show the greatest change in data due to fluence dependence. This proved fruitful because the average of the three pairs of excitation ended up being remarkably close to the  $\gamma$  obtained simply between the 50 nJ and 15 nJ pair. Thus it is expected in future studies that using excitation pairs with the greatest energy difference between them will yield the best values for annihilation. It should be remembered that the labels “50nJ” and “15nJ” refer to the energy measure at 420 nm at the sample position during experimentation using an Ophir® Nova II power meter.

Because the annihilation coefficient is now known (although it may contain significant error), the diffusion coefficient,  $D$ , can be calculated from the following equation:<sup>62,78,80-81</sup>

$$\gamma = 4\pi DR \quad (4-10)$$

Here, “ $R$ ” is the exciton annihilation radius, the distance at which annihilation is faster than diffusion.<sup>80</sup> The equation assumes that the excitons have to diffuse some distance before annihilation can occur. In the literature, Valencia et al. have assumed  $R$  to be the exciton delocalization length,<sup>81</sup> and Lewis et al. have found it using  $R = a(R_e/R_g)^{3/2}$ ,

where “a” is the interchain hopping distance,  $R_e$  is the Förster radius for ET onto the excited segment and  $R_g$  is the Förster radius for ET onto the ground state segment.<sup>80</sup> In general, most organic materials have Förster radii less than 5 nm,<sup>82</sup> but because they are not exactly known for the films studied here, a simple approach of assuming  $r = 6.0$  nm,<sup>23,62,75</sup> which is the length of one chromophore unit, or 5 PRUs, should give an decent upper estimate.

Equation 4-11 relates diffusion length ( $L_D$ ) to the known diffusion coefficient ( $D$ ), based on the unquenched fluorescence lifetime ( $\tau_{FL} = 550$  ps), taken from literature values of the PPE-SO<sub>3</sub> in water solution.<sup>13,26,30,62,75</sup> This solution lifetime was used because PPE-SO<sub>3</sub> is aggregated in water, and it appears that the films made, despite being made from methanol solutions, also exhibit strong aggregation.

$$L_D = \sqrt{d\tau D} \quad (4-11)$$

This model, based on random walk of the excitons, can be used for any dimensional diffusion because  $d$  is the dimensionality term. If one-dimensional diffusion is assumed,  $d = 1$ , if three-dimensional diffusion is assumed,  $d = 6$ . Here, if three-dimensional diffusion is assumed it allows for both interchain and intrachain diffusion to take place with equal probability. For the most part, interchain and intrachain diffusion take place at very different rates, and it is hard to model them together. Therefore, both dimensionalities are presented below. From Equation 4-11, values of  $L_D$  are summarized in Table 4-2, along with the values of variables and constants calculated up to this point.

Values of  $L_D$  on the order of magnitude of 1 to 100 nm are expected from reports of other conjugated polymers,<sup>13,26,30,51</sup> so  $L_D = 52.2$  nm is a reasonable value, but  $L_D =$

128 nm is extremely high, and is considered inaccurate. 52.2 nm may be a little on the high side compared to most singlet excitons, but that is good when dealing with solar cells where longer exciton diffusion is preferred. The distance of 52.2 nm in terms of number of bilayers from calculations from Table 2-1 (1.3 nm per layer) can be approximated to about 20 bilayers. However, this number is extremely unreliable, and no true conclusion should be drawn from it until further studies have verified these results. However, if the data and calculations are correct, then at least qualitatively one can say that in 20 bilayer PDDA/PPE-SO<sub>3</sub> films the excitons generated have a chance to diffuse through the CPE bilayers and reach the titania interface where they can cleave and undergo electron injection. Creating films with more than this number of bilayers would not improve collection efficiency or device performance.

Table 4-2. Calculation of diffusion length for 30 bilayer film.

$K_{50}$	$K_{30}$	$K_{15}$	$n_{50}^*$	$n_{30}^*$	$n_{15}^*$
17.82e12 s <sup>-1</sup>	13.05e12 s <sup>-1</sup>	10.10e12 s <sup>-1</sup>	2.93e19 cm <sup>-3</sup>	1.76e19cm <sup>-3</sup>	8.78e18cm <sup>-3</sup>
$\gamma$ (average)	R	D	$\tau_{FL}$	$L_D$ (d=1)	$L_D$ (d=6)
3.73e-7cm <sup>3</sup> s <sup>-1</sup>	6.0 nm	4.95e-2cm <sup>2</sup> s <sup>-1</sup>	550 ps	52.2 nm	128 nm

Once again, the errors which manifested themselves in these calculations included but were not limited to: low fluences creating low EEA and large amounts of noise, use of constants from solutions even though these are films, an estimation of the chromophore length to be 6.0 nm, and the use of that number as the annihilation radius. In the future, higher and more stable fluences and more accurate kinetic modeling should improve the calculations.

## Effect of Changing Number of Bilayers

Transient absorption experiments were run with 30, 20, 10, and 5 bilayer films to help confirm the dynamics seen on the pure 30 bilayer film. All data shown are the average of 10 scans, with 50 points taken at each time step. The best signal to noise ratios were obtained in the higher number of bilayer films, with decreasing resolution as the number of bilayers was reduced. This is because fewer photons were collected by the fewer number of bilayers, so there was a lower signal compared to the same amount of noise. Although it does not affect the data, it should be noted that “time zero” was shifted between previous and the following experimentations so that the peak excitation takes place at 0.2 instead of 0.9 ps on the time axis.

In Figure 4-11, the 30 bilayer film was excited with 12 nJ energy (the maximum attainable at the time) at 420 nm. All of the experiments in this section were run using that energy for consistency. In the left graph of Figure 4-11, three wavelengths corresponding to bleach (400, 425, and 450 nm) and three wavelengths corresponding to PIA (475, 525, and 575 nm) were plotted. Out of the bleach signals, 450 nm gave the largest magnitude upon initial excitation, while 400 nm, where the whitelight counts were lowest, shows considerable noise. The PIA signal curves are decidedly smaller amplitude than the 50 nJ test in Figure 4-3. Again, this is attributed to an undesirable lower irradiance from the pump.

On the right graph in Figure 4-11, the same TA data is plotted versus wavelength and specified times to show the dynamics. The bleach is still apparent, but the previously strong PIA at 475 nm is absent, while the rest of the PIA above 460 nm wavelengths appears but weakly. It is believed that the 475 nm PIA of singlet state PPE-SO<sub>3</sub> to a higher excited state is missing because the excitation energy is not

enough to generate as many excitons as the 50 nJ excitation did, so fewer excitons are around to absorb the 475 nm light.

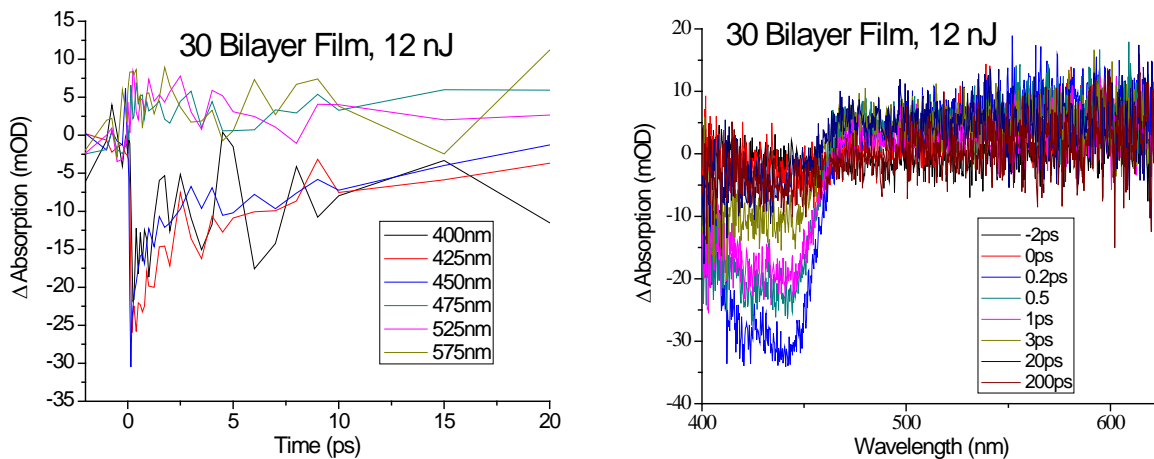


Figure 4-11. 30 bilayer film excited with 12 nJ. The left graph plots three bleach signals (400, 425, and 450 nm) and three PIA signals (475, 525, and 575 nm) versus time. The bleach signal to noise is better than the PIA signal's, and the fast component of bleach decay takes place within 5 ps. The right graph plots the wavelength spectrum at chosen times to show the dynamics.

Single exponential decays were fitted to the bleach signal for the first 5 ps for these data as a better visual reference than smoothing techniques. For 400 nm, the lifetime ( $\tau$ ) was 1.492 ps with an  $r^2 = 0.511$ , which indicates a poor fitting.  $r^2$  values approaching unity indicate perfect fit, so this  $r^2$  value for bleach decay signifies that the lifetime is likely incorrect. This is probably due to the poor signal to noise at the bleach wavelength of 400 nm. To improve this, lifetimes were calculated at 425 and 450 nm bleach signals, and gave 1.388 ps ( $r^2 = 0.825$ ) and 0.530 ps ( $r^2 = 0.922$ ). Thus, the better signal to noise at those wavelengths produced clearer exponential decay data.

Similarly, exponential decays of the PIA signals were fitted for the 475, 525, and 575 nm data. Only 575 nm gave a non-negligible value, and it was 6.553 ps ( $r^2 = 0.515$ ), which is a poor fitting, and can not be trusted.

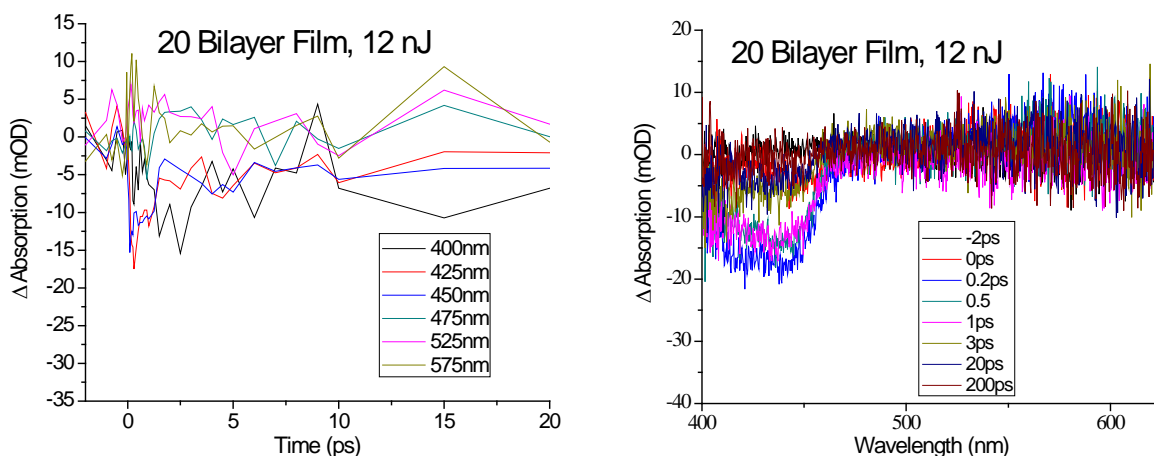


Figure 4-12. 20 bilayer film excited with 12 nJ at 420 nm. The left graph plots three bleach signals (400, 425, and 450 nm) and three PIA signals (475, 525, and 575 nm) versus time. Noise is considerable, yet bleach decay appears to take place within 5 ps. The right graph plots the wavelength spectrum at chosen times to show the dynamics.

In Figure 4-12, the TA data from the 20 bilayer film is plotted versus time and wavelength once again. Noise begins to become a bigger issue compared to the 30 bilayer film. Nevertheless, bleach lifetime decay components were obtained for the bleach signal at 425 nm and 450 nm as 0.735 ps ( $r^2 = 0.827$ ) and 0.851 ps ( $r^2 = 0.721$ ). Notably, the degree of fitness is worse, likely from the lower signal to noise ratio. Also, the only SE fit which could be obtained was  $\tau = 0.213$  with ( $r^2 = 0.433$ ) at 575 nm.

The bleach signal is still clear on the right graph in Figure 4-12, but this is not the case for the 10 bilayer film in Figure 4-13. Noise below 425 nm wavelengths appears as large as the true signal itself, reaching as low as -10 mOD, while PIA is all but impossible to evaluate. Looking at the time plot on the left of Figure 4-13, the highlighted 450 nm bleach decay is seen up to 5 ps. Fitting of these data with a single exponential decay over the first 5 ps yields  $\tau = 0.187$  ps ( $r^2 = 0.515$ ), which is very short compared to previous values.

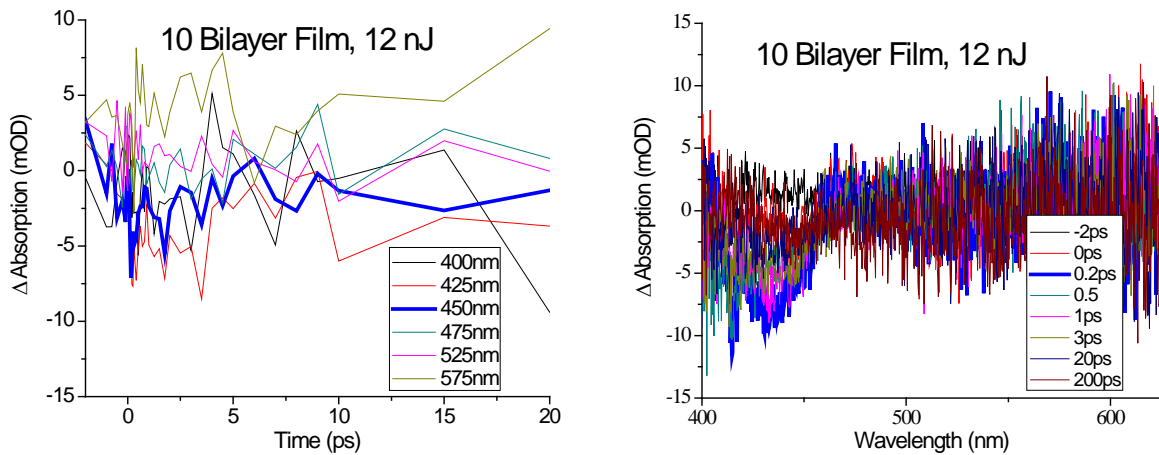


Figure 4-13. 10 bilayer film excited with 12 nJ at 420 nm. The left graph plots three bleach signals (400, 425, and 450 nm) and three PIA signals (475, 525, and 575 nm) versus time. Noise is very strong, yet bleach decay can be seen within 5 ps in the highlighted 450 nm data. The right graph plots the wavelength spectrum at chosen times to show the dynamics.

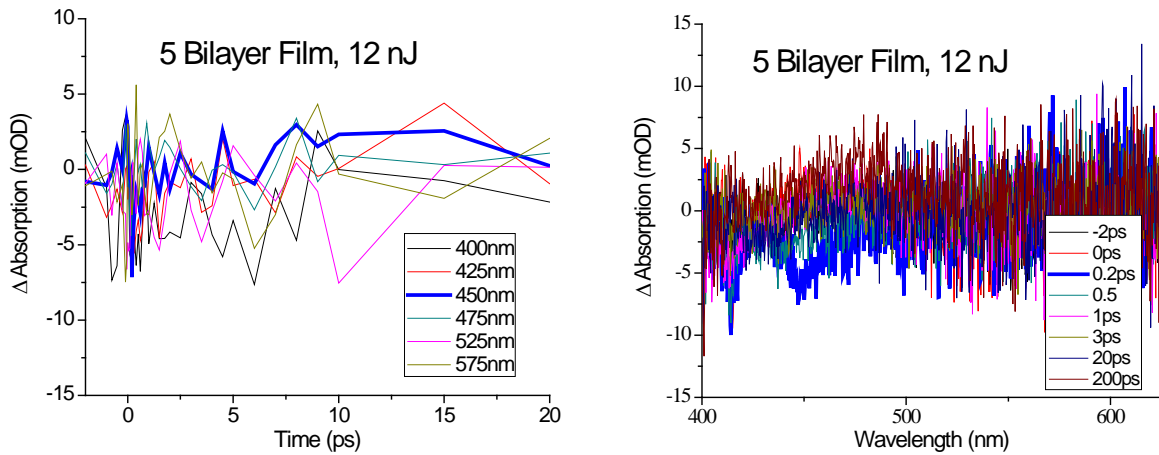


Figure 4-14. 5 bilayer film excited with 12 nJ at 420 nm. The left graph plots three bleach signals (400, 425, and 450 nm) and three PIA signals (475, 525, and 575 nm) versus time. Signal to noise is considerable, yet bleach decay appears to take place within 5 ps. The right graph plots the wavelength spectrum at chosen times to show the dynamics.

One would think that the trend of decreasing signal to noise with decreasing bilayer count would make the 5 bilayer film uninteresting if not unreadable. However, in Figure 4-14, an interesting band was detected. Unaggregated stimulated emission

within the first picosecond was observed as a negative signal around 450 nm. As previously noted, this corresponds to unaggregated PPE-SO<sub>3</sub> stimulated emission. This is very interesting because this signal was not seen in any of the other bilayer films. The 450 nm signal must mean that the polymer exists with little or no aggregation at 5 bilayers, which is logical because aggregation has been shown not to form until many bilayers are built-up and the polymers have had opportunity to interact and  $\pi$ -stack with neighbor chains, for instance.<sup>51</sup> Thus, when finding the bleach lifetime of the 5 bilayer film at 450 nm, an unexpectedly good fitting was obtained, with  $\tau = 0.207$  ps.

Table 4-3 summarizes the lifetimes obtained at the selected bleach and PIA signals of 425, 450, 475, and 575 nm for the 4 types of bilayer films. 525 nm was also fit, but produced no real numbers. In general, the higher the BL number, the better the data's signal to noise, and hence the better the fit and the higher the  $r^2$  value. As noted before, the 450 nm signal for the unaggregated 5 bilayer film shows a stimulated emission signal.

Table 4-3. Lifetimes of states using single exponential decay fittings.

BL	$\tau_{425\text{nm}}$ ( $r^2$ )	$\tau_{450\text{nm}}$ ( $r^2$ )	$\tau_{475\text{nm}}$ ( $r^2$ )	$\tau_{575\text{nm}}$ ( $r^2$ )
30	1.388ps (0.825)	0.530ps (0.922)	-	6.553ps (0.515)
20	0.735ps (0.827)	0.851ps (0.721)	-	0.213ps (0.433)
10	-	0.187ps (0.587)	0.524ps (0.080)	-
5	-	0.207ps (0.729)	6.99ps (0.191)	-

## CHAPTER 5 CONCLUSIONS AND FUTURE WORK

### **Experimental Discussion**

To keep the films as fresh as possible, they were stored in a vacuum desiccator when not in use; however, while on the TA set-up, they were exposed to the atmosphere. Because it took several days to reach the optimal TA setting, water in the air may have degraded the titania structure, even at the low pressures in the desiccator. Also, the films were dried for 12 hours between coatings of 10 bilayers, but whenever possible, all layers made in the future should be coated in a single trial. Humidity must be kept at a minimum.

The rotating stage proved fruitful, and tape held the films to the back of it surprisingly well. The only trouble was in finding the correct overlap position of pump and probe on the thin film. This was accomplished by alignment through a 100  $\mu\text{m}$  pinhole (inside the circular rotating cell, but not rotating) while detecting with a photodiode/oscilloscope placed behind the pinhole and adjusting the probe white light to go through the center. Then, without moving the stationary pinhole, the pump beam was aligned through it. Finally, the entire stage was translated along the beam axis a measured number of millimeters to place the taped film at the previous pinhole position.

Additionally, a major problem was discovered part way through experimentation with the optical delay stage. It appeared that somehow it was changing alignment as it moved, which meant at long timescales a reproducible decay due to loss of overlap was constantly seen. To fix this problem, two TA set-up mirrors before the optical delay stage were iteratively adjusted while the beam after the stage, measured at long distances (taken to a far wall with an inserted mirror), was monitored. To check that it

was fixed, a solution of perylene was used as the sample and near constant bleach signal was seen due to the long lifetime the molecule. Because the optical delay stage problem only became significant at longer (>100 ps) timescales, shorter timescales, measured in this paper, were ultimately unaffected and are still considered reliable.

The generation of white light for the probe also became a problem, as part way through experimentation the CaF<sub>2</sub> rotating stage power supply was lost. Apparently, the original power supply was much too powerful for the little rotating motor, so a new power supply, which uses less than 5 V, was installed. It was actually connected in parallel with the homemade sample rotating stage motor, which makes experimentation more streamlined. The CaF<sub>2</sub> window was also replaced, changing the whitelight counts.

The grating inside the Andor iStar Shamrock also gave trouble. In the first few experiments, it detected the 420 nm pump scatter signal at values closer to 414 nm. Not only that, but the detected wavelength actually *changed* upon moving the diffraction grating range. This is a serious problem which was discovered to be caused by an internal, computer-controlled sine-bar which controls the grating. If this were a mechanical sine-bar, it could have been fixed by hand, but because it is internally controlled it instead requires the whole Shamrock be sent to the company for fixing. In lieu of that down time, the grating was fixed to the range of ~360 nm to ~630 nm, and calibrated once with a Mercury lamp.

### **Future Experiments**

Some conditions which could have an affect on the results are temperature and wait time between creating the films and testing them. To control these variables, future tests should be done at constant room temperature for optimum laser operating stability conditions (to avoid Florida summer weather dependence fluctuations). Stable pressure

and humidity would also help, and all tests should be done within one week after the films have been prepared. As it was, the Tsunami and Spitfire had to constantly be monitored and adjusted, which could have been avoided with favorable room stability. And even though auto-correlation experiments were run to check the Spitfire pulse width, constant adjustment meant variable instrument response functions in these experiments.

Further areas of testing the PPE-SO<sub>3</sub>/TiO<sub>2</sub>/FTO glass films include experiments at lower temperatures, which would limit the exciton diffusion to its "downhill migration" only, in which excitons travel to lower energy states until they reach the one of greatest population.<sup>13,23</sup> At the lower temperatures, they would be "trapped" and kept from further "hopping" to other states.<sup>23</sup> So in the tests performed in the work of this paper at room temperature, a second, thermally activated hopping process likely contributed a second component to the exciton diffusion.

Currently, numerous organic conducting polymers are being developed for use in optoelectronic devices.<sup>57-60,68</sup> A new set of poly(arylene ethynylene) conjugated polymers with carboxylic side groups has been developed at the University of Florida, and preliminary studies have been done. The author of this manuscript was also working on characterizing the ultrafast photo-dynamics of those carboxylates at the time of this publication. Additional work to follow this paper would include tests over that entire family of polyelectrolytes (each with slight changes in monomer length or substituents) to evaluate the validity of the diffusion equations and to determine best choice of sensitizer in polymer-sensitized solar cells.

As mentioned before, there are multiple ways to calculate exciton diffusion length, and one of those ways relies on calculating fluorescence lifetimes in the steady state in the presence and absence of a quencher. Titania acts as quencher, but films without it, or some kind of scaffold to create a mesoporous adsorption surface for increased polymer deposition for TA detection, could not act as a background signal for the unquenched calculations. Therefore, a similar nanoparticle or surface must be developed or found which can act as titania for structural purposes, but not be involved in any sort of quenching. The search for such a material will be analyzed based on the literature, and more importantly, on TA experiments which try them.

From the data collected in this paper, the bleach signal was clear, as is a photo-induced absorption into an excited state. But to truly determine which stimulated emission process appears (from PPE-SO<sub>3</sub> or TiO<sub>2</sub>) additional tests would need to be done which include probing higher wavelengths or conducting photocurrent studies. Instead of changing the grating diffraction angle to not select lower wavelengths studied in this paper, it is instead proposed that the grating be changed altogether. The current set-up grating is 300 lines/mm, so to increase the wavelength range of signal detection, a grating with fewer lines/mm should be used.

Additionally, a technique known as Singular Value Decomposition (SVD) has been developed to separate multiple signals, like those that appeared in the TA data.<sup>77</sup> The author of this paper has been researching the method, and plans to use it to separate the components of bleach, PIA, and SE. Ideally, though, averaging of more than 10 data sets and using higher energies would improve the signal to noise ratio, and may be needed to get useful SVD results.

## Conclusions

### Exciton Diffusion Calculations

In conjunction with using computer software to calculate derivatives of the smoothings of the films at different pump excitation energies, exciton-exciton annihilation formulas were evaluated and a diffusion coefficient ( $D$ ) of  $4.95 \times 10^{-2} \text{ cm}^2 \text{ s}^{-1}$  and a one-dimensional diffusion length ( $L_D$ ) of 52.2 nm were found. 52.2 nm qualitatively corresponds to about 20 bilayers, so that is the proposed limit of efficient build-up of bilayers to improve light collection for use in solar cells. It needs to be noted that it is only a rough estimate because of all of the approximations which were made in the calculations.

To find the numbers above, the thickness of the CPE films were not taken as close to that of the pure titania thickness (1.6 microns), but instead were calculated to be 41 nm for the PPE-SO<sub>3</sub> layers in the 30 bilayer film. Additionally, the annihilation radius,  $R$ , could in the future be based on calculated Förster radii for energy transfer between two polymer segments, but here was based on the assumption found in the literature that the annihilation radius equals one chromophore unit, which is 5 PRUs for PPE-SO<sub>3</sub> and corresponds to 6.0 nm.<sup>81</sup> The diffusion length found is higher than values for many singlet excitons,<sup>51</sup> which can be attributed to assuming a cylindrical (and therefore smaller) absorption volume and because the excitation energies (50, 30, and 15 nJ) could have been higher to give clearer exciton-exciton annihilation. Furthermore, based on the model,<sup>62</sup> other deactivation mechanisms were not explicitly accounted for, which may be necessary to further refine the calculations. These include the true effect of TiO<sub>2</sub> quenching and quenching by other traps and structural centers within the film.

## **PPE-SO<sub>3</sub> Bilayer Film Dynamics**

To summarize, films of 5, 10, 20, and 30 bilayers were fabricated and tested using TA. The trend was that a greater number of bilayers showed greater signal, with the 30 bilayer film showing the strongest signals. The bleach lifetime of that film measured at 450 nm was found to be 530 fs, giving the best fit of any of the lifetimes calculated. Most lifetimes were less than 1 ps, but due to low energy of excitation, signal to noise was considerable and exponential decay fitting was mostly unreliable at the lower number of bilayers. However, one interesting finding was that the 5 bilayer film showed stimulated emission from the unaggregated form of PPE-SO<sub>3</sub>, which did not occur in any other film. It is therefore determined that somewhere between 5 and 10 bilayers aggregation becomes dominant in these films. This can be reaffirmed within the literature.<sup>15-16</sup>

## **Solar Cells**

In the future, design of optimal polymers from theory (calculating the HOMO and LUMO levels)<sup>31,37,46</sup> and novel synthetic techniques to make them will provide an increasing need to understand experimentally the photophysical properties of conjugated polyelectrolytes in films. Transient Absorption is a useful technique for understanding these properties, and has been proven to be promising once again. It is hoped that together in the future, theory and experiment can determine optimal compositions for solar cells and other devices, which can then be used to solve the energy crisis through intelligent product designs that can be implemented with confidence.

## LIST OF REFERENCES

1. U.S. Department of Energy website. U.S. Department of Energy. 2009. 10/7/2009. <http://www.energy.gov>.
2. *The Future of Power and Energy in the World*. Lewis, Nate. Presentation. 2004. 10/24/2009. <http://online.kitp.ucsb.edu/online/colloq/lewis1/>.
3. Sze, S. M. and Ng, Kwok K. *Physics of Semiconductor Devices*; Wiley: Hoboken, NJ, 2007.
4. *Reference Solar Spectral Irradiance: Air Mass 1.5*. NREL. 2008. 10/23/2009 <http://rredc.nrel.gov/solar/spectra/am1.5/>.
5. Green, Martin A.; Emery, Keith; Hishikawa, Yoshihiro; Warta, Wilhelm. *Progress in Photovoltaics: Research and Applications*; **2008**, 16, 435-440.
6. Grätzel, Michael. *Chemistry Letters* **2005**, 34(1), 8-13.
7. Grätzel, Michael. "Photoelectrochemical Solar Conversion by Dye Sensitization." *Future Generation Photovoltaic Technologies: First NREL Conference*; American Institute of Physics: Woodbury, NY, 1997.
8. Grätzel, Michael. *Journal of Photochemistry and Photobiology A: Chemistry* **2004**, 164, 3-14.
9. O'Regan, Brian and Grätzel, Michael. *Nature* **1991**, 353, 737-740.
10. Grätzel, Michael. *Nature* **2001**, 414, 338-344.
11. Wang, Mingkui; Chen, Peter; Humphry-Baker, Robin; Zakeeruddin, Shaik; Grätzel, Michael. *ChemPhysChem* **2009**, 10, 290-299.
12. Kim, Sanghoon; Lee, Jae Kwan; Kang, Sang Ook; Ko, Jaejung; Yum, J. H.; Fantacci, Simona; De Angelis, Filippo; Di Censo, D.; Nazeeruddin, Md. K.; Grätzel, Michael. *JACS* **2006**, 128, 16701-16707.
13. Mikhnenko, O. V.; Cordella, F.; Sieval, A. B.; Hummelen, J. C.; Blom, P.W.M.; and Loi, M. *Journal of Physical Chemistry B* **2008**, 112, 11601-11604.
14. Baur, Jeffery; Rubner, Michael F.; Reynolds, John R.; Kim, Seungho. *Langmuir* **1999**, 15, 6460-6469.
15. Tan, Chunyan; Pinto, Mauricio R.; Schanze, Kirk S. *Chemical Communications* **2002**, 5, 446-447.

16. Mwaura, Jeremiah K.; Pinto, Mauricio R.; Witker, David; Ananthakrishnan, Nisha; Schanze, Kirk S.; Reynolds, John R. *Langmuir* **2005**, *21*, 10119-10126.
17. Mwaura, Jeremiah K.; Zhao, Xiaoyong; Jiang, Hui; Schanze, Kirk S.; Reynolds, John R. *Chemical Materials* **2006**, *18*, 6109-6111.
18. Ramey, Michael B.; Hiller, Jeri'Ann; Rubner, Michael F.; Tan, Chunyan; Schanze, Kirk S.; Reynolds, John R. *Macromolecules* **2005**, *38*, 234-243.
19. Taranekar, Prasad; Qiao, Qiquan; Jiang, Hui; Ghiviriga, Ion; Schanze, Kirk S.; Reynolds, John R. *JACS* **2007**, *129*, 8958-8959.
20. Furukawa, Naoki; Mair, Chad E.; Takeda, Jun; Kleiman, Valeria D. *Applied Physics Letters* **2004**, *85*(20), 4645-4647.
21. Tan, Chunyan; Atas, Evrim; Müller, Jürgen G.; Pinto, Mauricio R.; Kleiman, Valeria D.; Schanze, Kirk S. *JACS* **2004**, *126*, 13685-13694.
22. Hardison, Lindsay M.; Zhao, Xiaoyong; Jiang, Hui; Schanze, Kirk S.; Kleiman, Valeria D. *Journal of Physical Chemistry C* **2008**, *112*, 16140-16147.
23. Müller, Jürgen G.; Tan, Chunyan; Atas, Evrim; Kleiman, Valeria D.; Schanze, Kirk S. *JACS* **2006**, *128*, 4007-4016.
24. Müller, J. G.; Lupton, J. M.; Feldmann, J. *Physical Review B* **2005**, *72*, 195208.
25. Müller, J. G.; Lemmer, U.; Raschke, G.; Anni, M.; Scherf, U.; Lupton, J. M.; Feldmann, J. *Physical Review Letters* **2003**, *91*(26), 267403.
26. Holzhey, A.; Urich, C.; Brier, E.; Reinhold, E.; Bäuerle, P.; Leo, K.; Hoffman, Michael. *Journal of Applied Physics* **2008**, *104*, 064510.
27. Fahmi, Adil; Minot, Christian. *Surface Science* **1994**, *304*(3), 343-359.
28. Lorenc, M.; Ziolk, M.; Naskrecki, R.; Karolczak, J.; Kubicki, J.; Maciejewski, A. *Applied Physics B* **2002**, *74*, 19-27.
29. Nelson, Jenny. *Physical Review B* **1999**, *59*(23), 15374-15380.
30. Scully, Shawn R. and McGehee, Michael D. *Journal of Applied Physics* **2006**, *100*, 034907.
31. Hagberg, Daniel P.; Marindo, Tannia; Karlsson, Karl Martin; Nonomura, Kazuteru; Qin, Peng; Boschloo, Gerrit; Brinck, Tore; Hagfeldt, Anders; and Sun, Licheng. *Journal of Organic Chemistry* **2007**, *72*, 9550-9556.

32. Henry, C. H. *Journal of Applied Physics* **1980**, 51(8), 4494-4499.
33. Westenhoff, Sebastian; Howard, Ian A.; Hodgkiss, Justin M.; Kirov, Kiril R.; Bronstein, Hugo A.; Williams, Charlotte K.; Greenham, Neil C.; and Friend, Richard H. *JACS* **2008**, 130, 13653-13658.
34. Ai, Xin; Guo, Jianchang; Anderson, Neil A.; and Lian, Tuanquan. *Journal of Physical Chemistry B* **2004**, 108, 12795-12803.
35. Gilot, Jan; Barbu, Ionut; Wienk, Martijn M.; Janssen, René A. J. *Applied Physics Letters* **2007**, 91, 113520.
36. Veldman, Dirk; Bastiaansen, J. A. M.; Langeveld-Voss, Bea; Sweelssen, Jörgen; Koetse, Marc M.; Meskers, Stefan C. J.; Janssen, René A. J. *Thin Solid Films*. **2006**, 511-512, 581-586.
37. Meskers, Stefan C. J.; Hübner, Jens; Oestreich, Michael; Bassler, Heinz. *The Journal of Physical Chemistry B* **2001**, 105, 9139.
38. Gilot, Jan; Wienk, Martijn M.; Janssen, René A. J. *Applied Physics Letters*. **2007**, 90, 143512.
39. Lanzani, G.; Cabanillas-Gonzalez, J.; Virgili, T.; Yeates, S.; Ariu, M.; Nelson, J.; Bradley, D. D. C. *Physical Review B* **2005**, 71, 014211.
40. Gadermaier, Christoph; Lanzani, Guglielmo. *Journal of Physics: Condensed Matter* **2002**, 14, 9785-9802.
41. Sessi, P.; Brambilla, A; Finazzi, M.; Duò, L.; Cabanillas-Gonzalez, J.; Egelhaaf, H. J.; Ciccacci, F.; Lanzani, G. *Journal of Chemical Physics* **2008**, 128, 65-67.
42. Ghosh, Hirendra Nath. *BARC Newsletter: Founder's Day Special Issue* **2001**, 94-100.
43. Yang, Shujiang; Olishevski, Pavel; Kertesz, Miklos. *Synthetic Metals* **2004**, 141, 171-177.
44. Wakizaka, Daiki; Fushimi, Toshiki; Ohkita, Hideo; and Ito, Shinzaburo. *Polymer* **2004**, 45(25), 8561-8565.
45. Drori, T.; Sheng, C.-X.; Ndobe, A.; Singh, S.; Holt, J.; Vardeny, Z. V. *Physical Review Letters* **2008**, 101, 037401.
46. Beljonne, D.; Pourtols, G.; Silva, C.; Hennebicq, E; Herz, L. M.; Friend, R. H.; Scholes, G. D.; Setayesh, S.; Müllen, K.; Brédas, J. L. *PNAS* **2002**, 99, 10982-10987.

47. Heeger, A. J.; Kivelson, S.; Schrieffer, J. R.; Su, W.-P. *Review of Modern Physics* **1988**, *60*(3), 781-851.
48. Wunnicke, O.; Müller-Buschbaum, P.; Wolkenhauer, M.; Lorenz-Haas, C.; Cubitt, R.; Leiner, V.; Stamm, M. *Langmuir* **2003**, *19*, 8511-8520.
49. Ariga, K.; Hill, J.; Ji, Q. *Physical Chemistry Chemical Physics* **2007**, *9*(19), 2319-2340.
50. Atas, Evrim. "Ultrafast Time Resolved Dynamics in Conjugated Dendrimers." Thesis. University of Florida, 2006.
51. Vella, Jarrett. "Singlet and Triplet Excitons in Organic and Organometallic Thin Films: Diffusion and Triplet Sensization." Thesis. University of Florida 2009.
52. Bricaud, Quentin, John R. Reynolds post-doctoral associate. "Department of Energy Meeting." Personal communication. 9 April 2009.
53. Bube, Richard H. *Photovoltaic Materials*; Imperial College Press: Stanford, CA, 1998.
54. Valeur, B. *Molecular Fluorescence: Principles and Applications*. Wiley: New York, NY, 2002.
55. Forrest, S. R.; Giebink, N. C.; Sun Y. *Organic Electronics* **2006**, *7*, 375-386.
56. Yamamoto, M.; Tsuchida, A.; Liebe, W.; Burkhart, R.; Tsubakiyama, K. *Macromolecules*. **1996**, *29*, 1589-1594.
57. Arys, X.; Laschewsky, A.; Jonas, A. M. *Macromolecules* **2001**, *34*, 3318-3330.
58. Liu, G. M.; Zhao, J. P.; Sun, Q. Y.; Zhang, G. Z. *J. Phys. Chem. B* **2008**, *112*, 3333-3338.
59. Jourdainne, L.; Lecuyer, S.; Arntz, Y.; Picart, C.; Schaaf, P.; Senger, B.; Voegel, J. C.; Lavallo, P.; Charitat, T. *Langmuir* **2008**, *24*, 7842-7847.
60. Caruso, F.; Niikura, K.; Furlong, D. N.; Okahata, Y. *Langmuir* **1997**, *13*, 3422-3426.
61. Sundström, V.; Benko, G.; Myllyperkiö, P.; Pan, J.; Yartsev, P. *JACS*. **2003**, *125*, 1118-1119.
62. Gulbinas, V.; Sundström, V.; Mineviciute, I.; Hertel, D.; Wellander, R.; Yartsev, A. *Journal of Chemical Physics* **2007**, *127*, 144907.

63. Sundström, V.; Westenhoff, S.; Beenken, W.; Friend, R.; Greenham, N.; Yarsev, A. *Physical Review Letters* **2006**, *97*, 166804.
64. Sundström, V.; Jespersen, K.; Beenken, W.; Zaushitsyn, Y.; Yartsev, A.; Andersson, M.; Pullerits, T. *Journal of Chemical Physics*. **2004**, *121*(24), 12613-12617.
65. Sundström, V.; Hilgenforff, M. *Journal of Physical Chemistry B* **1998**, *102*, 10505-10514.
66. Gratzel, M.; Hagfeldt, A. *Chemical Reviews* **1995**, *95*(1), 49-68.
67. Gratzel, M.; Rothenberger, G.; Moser, J.; Serpone, N.; Sharma, D. *JACS* **1985**, *107*(26), 8054-8059.
68. Schanze, K. S.; Reynolds, J. R.; Jiang, H.; Zhao, X.; Shelton, A.; Lee, S. H. *ACS Applied Materials and Interfaces* **2009**, *1*(2), 381-387.
69. Snook, J. H.; Samuelson, L.; Kumar, J.; Kim, Y-G.; Witten, J. *Organics Electronics* **2005**, *6*, 55-64.
70. Schwartz, B.; Smith, A.; Martini, I. *Physical Review B* **2004**, *69*, 035204.
71. Anderson, A.; Johansson, N.; Broms, P.; Yu, N.; Lupo, D.; Salaneck, W. R. *Advanced Materials* **1998**, *10*(11), 859-863.
72. Malone, W. M.; Albert, R. *Journal of Applied Polymer Science* **1973**, *17*(8), 2457-2461.
73. Kenkre, V.; Reineker, P.; *Exciton Dynamics in Molecular Crystals and Aggregates*; Springer: New York, NY, 1982.
74. Davydov, A. S. *Theory of Molecular Excitons*; McGraw-Hill: New York, NY, 1962.
75. Tan, Chunyan. "Conjugated Polyelectrolytes: Amplified Quenching, Self-Assembly and Sensor Applications." Thesis. University of Florida, 2004.
76. Schanze, K. S.; Reynolds, J. R.; Kleiman, V. D.; Zhao, X.; Pinto, M.; Hardison, L.; Mwaura, J.; Muller, J.; Jiang, H.; Witker, D. *Macromolecules* **2006**, *39*, 6355-6366.
77. Altan, Aysun. "Ultrafast Studies of a Photochromic Oxazine in Solution." Thesis. University of Florida, 2009.
78. Suna, A. *Physical Review B* **1970**, *1*(4), 1716.
79. Craig, D. P. and Walmsley, S. H. *Excitons in Molecular Crystals*; W. A. Benjamin, Inc.: New York, NY, 1968.

80. Lewis, A. J.; Ruseckas, A.; Gaudin, O. P. M.; Webster, G. R.; Burn, P. L.; Samuel, I. D. W. *Organic Electronics* **2006**, 7, 452-456.
81. Valencia, V. S.; Kepler, R. G.; Jacobs, S. J.; Beeson, P. M. *Exciton Annihilation Studies in Poly(p-Phenylene Vinylene)*; Donnelly Corporation: Tucson, AZ, 1995.
82. Lakowicz, J. R.; *Principles of Fluorescence Spectroscopy*; Kluwer Academic / Plenum Press: New York, NY, 1999.

## BIOGRAPHICAL SKETCH

Derek Austin LaMontagne was born in State College, Pennsylvania, in the autumn of 1985. He was raised in New Hampshire and Florida, where he learned to appreciate politics, art, sports, and science. In high school, he played varsity baseball and graduated valedictorian in 2003, earning an International Baccalaureate diploma.

He got his Bachelor of Science degree in chemistry and mathematics from the College of William and Mary in Virginia in 2006 after three years of study, during which time he did research for Dr. David Thompson and Dr. Junping Shi. He then immediately enrolled in the chemistry graduate program at the University of Florida. There he joined Dr. Valeria Kleiman's physical chemistry research group in 2007.

He enjoys and still plays many sports, especially saber fencing, through which he has competed with the W&M and UF teams. He has won many tournaments, and enjoys teaching the sport to undergraduates at UF.

He hopes to continue on at UF to get his doctorate. He also hopes to some day go to Mars, save the environment, and become President of the United States of America.